IEEE JOURNAL OF EMERGING AND SELECTED TOPICS IN POWER ELECTRONICS

Load Balancing of a Modular Multilevel Grid Interface Converter for Transformer-Less Large-Scale Wireless Electric Vehicle Charging Infrastructure

Giuseppe Guidi, *Senior Member, IEEE*, Salvatore D'Arco, Koudai Nishikawa and Jon Are Suul, *Member, IEEE*

***Abstract*-- This paper analyses the requirements for load balancing of a new transformer-less grid interface topology for large-scale electric vehicle (EV) charging infrastructures. The proposed configuration utilizes a Modular Multilevel Converter (MMC) to supply wireless EV chargers from each module. The inherent galvanic isolation provided by wireless inductive power transfer and the scalability of the MMC topology enable transformer-less connection to medium voltage (MV) distribution grids. This can reduce the footprint and copper volume of the internal power distribution for the parking infrastructure. The load distribution within the MMC topology depends on the location and power requirements of each EV to be charged. Requirements for load balancing by controlling the internal circulating currents of the proposed topology when supplying unevenly distributed loads are derived. It is also demonstrated how a second harmonic component of the circulating currents can be utilized to ensure balancing capability within each MMC arm, and how its required amplitude depends on the load distribution. The theoretical analysis and the performance of a corresponding control strategy are first verified by time-domain simulations of a large-scale infrastructure. Experimental results from a small-scale prototype based on an MMC where each arm has 12 modules with individual controllable loads are presented.**

***Index Terms*—Electric Vehicle Charging Infrastructure, Modular Multilevel Converters, Transformer-less Grid Interface, Wireless Power Transfer.**

Manuscript received May 26, 2020; revised August 10, 2020 and October 9, 2020; accepted November 13, 2020. Date of publication xx December 2020; date of current version xx xx 2021. The work was supported by the project "Modular Megawatt-range Wireless EV Charging Infrastructure Providing Smart Grid Services" (MoMeWeC), funded by the Research Council of Norway under the EIG CONCERT Japan program, Joint Call on Efficient Energy Storage and Distribution, with project number 284231, and by the project "Grid and Charging Infrastructure of the Future" (FuChar) funded by the Research Council of Norway and industry partners under the ENERGIX program, with project number 295133. Recommended for publication by Associate Editor NN. (*Corresponding author: Jon Are Suul.*)

G. Guidi and S. D'Arco are with SINTEF Energy Research, 7465 Trondheim, Norway (e-mail: Giuseppe.Guidi@sintef.no, salvatore.darco@sintef.no).

K Nishikawa is with the Department of Electrical, Electronics and Information Engineering, Nagaoka University of Technology, Niigata 940-2188, Japan, (e-mail: knishikawa@stn.nagaokaut.ac.jp).

J. A. Suul is with SINTEF Energy Research, 7465 Trondheim, Norway, and also with the Department of Engineering Cybernetics, NTNU, 7491 Trondheim, Norway (e-mail: Jon.A.Suul@sintef.no).

Color versions of one or more of the figures in this paper are available online at http://ieeexplore.ieee.org.

Digital Object Identifier xx.xxxx/JESTPE.2020.xxxxxxx

NOMENCLATURE

Main variables and parameters

Upper case symbols represent quantities in the SI system
Lower case symbols represent per unit quantities
Italic bold fonts represent phasor or complex quantities

V	Voltage
I	Current
P, Q	Active, Reactive power
L, C, X	Inductance, Capacitance, Reactance
N	Number of modules per arm
d	Insertion index for arm or module
T	Period of the fundamental frequency
k_v	Voltage margin
k_m	Safety margin

Subscripts

a,b,c,x	Phases a,b,c or unspecifies phase x
u,l,y	Upper or lower arm or unspecified arm y
dc	Direct component
ω	Fundamental frequency component
$2\,\omega$	Second harmonic component
B	Base value for per unit system
$+,-,z$	Positive, Negative, Zero sequence component
dq	Direct and quadrature axis components
$\alpha\beta$	Stationary frame orthogonal components
eq	Equivalent arm component
nom	Rated value

Superscripts

M	Reference to generic module
M_i	Reference to ith module in the arm
σ	Internal arm sum. $\sum_{i=1}^{N} \square^{M_i}$ except $d^{\sigma} = \frac{1}{N}\sum_{i=1}^{N} d^{M_i}$
Σ	$(\square_u + \square_l)/2$
Δ	$\square_u - \square_l$ except for v and p given by $(\square_u - \square_l)/2$
*	Reference value for control

Symbol modifiers

$\hat{\square}$	Amplitude of three phase quantity
$\breve{\square}$	Complex conjugate
$\overline{\square}$	Average value
$\dot{\square}$	Time derivative

I. INTRODUCTION

Electrification of road transport is an essential step towards reaching national and international targets for reduction of CO2 emissions. An increasing number of electric vehicles (EVs) resulting from this development trend is expected to generate a need for large-scale EV charging facilities [1], [2]. Such infrastructures should be capable of simultaneously charging several hundreds, or even more than a thousand, EVs and will require high-power installations in the multi-megawatt range [2]-[6]. Especially for large residential parking areas in space-constrained urban areas, the compactness of the electrical installations can be of critical importance.

Currently, Inductive Power Transfer (IPT) technology for wireless charging of EVs is gaining acceptance as a preferred solution in terms of user convenience and as an enabling technology for future self-driving and autonomous vehicles [7]-[9]. By eliminating the need for direct electrical connections and by fully integrating the charging unit below the surface of a parking slot, wireless EV charging can provide a safe, reliable, robust and easily automated charging interface suitable for a public infrastructure. Furthermore, the lack of physical contact between the sending and receiving sides of the charging system ensures inherent galvanic isolation.

This paper presents a system configuration for a large-scale EV charging infrastructure that takes advantage of the galvanic isolation provided by IPT technology to reduce the footprint of the electrical installation by enabling modular and transformer-less integration with the distribution network. The studied topology was first proposed in [10] and is based on the modular multilevel converter (MMC) for interfacing directly with the medium voltage (MV) distribution grid. Each module of the MMC is then equipped with a wireless EV charger operating at a floating electrical potential. The voltage rating for the grid interface can be easily scaled by the number of modules in each phase of the MMC, as long as the power converters of each module as well as the resonant network and the coils for the wireless power transfer are sufficiently insulated with respect to ground.

The proposed system configuration is partly inspired by previous studies of modular converter topologies utilized for grid integration of energy storage systems with low voltage battery modules at floating potential [11], [12]. Similar configurations have been recently studied for photovoltaic (PV) generation at floating potential [13], [14], and for EV battery charging [15], [16], but without considering the need for galvanic isolation. The possibility of introducing power sources or loads in each module of modular converters has also been considered for solid-state transformers (SSTs) [17]-[19]. Furthermore, MMC-based configurations with high frequency transformers for providing galvanic isolation have been proposed for solar PV generation [20] and as grid interfaces of modular systems for inductive power transfer [21]-[23]. However, most of these applications assume a controllable or evenly distributed loading of the modules constituting the MMC topology. By contrast, the application proposed in this paper implies that an arbitrary number of modules can be fully loaded, disconnected or operating at partial load, depending on the presence and charging needs of the EVs. This introduces additional challenges for the power management of the system.

The first main contribution of this paper is the introduction of the MMC based grid interface for wireless EV chargers, where a charger can be supplied by each module to enable a large-scale transformer-less charging infrastructure. The discussion of this concept as first proposed in [10] is expanded with a qualitative assessment of the hardware and control requirements and by a simplified calculation of the potential benefits is terms of copper volume needed for the power distribution in the parking infrastructure. The second main contribution of the paper is the analysis of the balancing requirements for MMC applications with individually loaded modules, including a method for calculating the second harmonic circulating current that will ensure intra-arm balancing capability. This analysis is motivated by the operative constraints of this proposed system configuration but can be generalized to any other application of MMCs with unbalanced load or generation in the individual modules.

The paper is structured as follows. Section II introduces and discusses the concept of the proposed MMC-based EV charging system and includes a simplified quantification of the possible copper savings compared to a conventional scheme. Based on [10], a more detailed analysis of the requirements for balancing of unevenly distributed loads within the MMC topology is presented in section III, while the associated control functions are discussed in section IV. Section V is dedicated to the analysis of the intra-arm balancing of the converter topology and the derivation of how intra-arm balancing capability can be ensured by injection of a second harmonic circulating current. In section VI, the impact of the balancing control on the conduction losses of the converter topology is analyzed. Section VII presents simulation results obtained for an envisioned large-scale infrastructure with 300 parking slots for wireless EV charging as an illustration of the operability of the proposed concept and the validity of the control approach. Further verifications are provided in section VIII by experimental results obtained with a small-scale prototype of an MMC with 12 modules per arm and individually controllable loads integrated in each module.

II. CHARGING STATION TOPOLOGY

Commercially available EV chargers are designed for being supplied from low voltage ac grids [24]. Thus, application in large-scale charging infrastructures would result in the configuration reported in Fig. 1, with charger units (either wireless or conventional) organized in groups. Each group of chargers is supplied by an internal low voltage (LV) ac bus, with a dedicated transformer for connection to the medium voltage (MV) distribution system [6]. The number of charging units that can be parallel-connected in each group is limited by the capacity of the low-voltage bus and by the rating of the MV/LV transformer. The main drawbacks of this conventional layout are associated to the dimensioning of the low voltage ac-buses for high currents, resulting in heavier and more

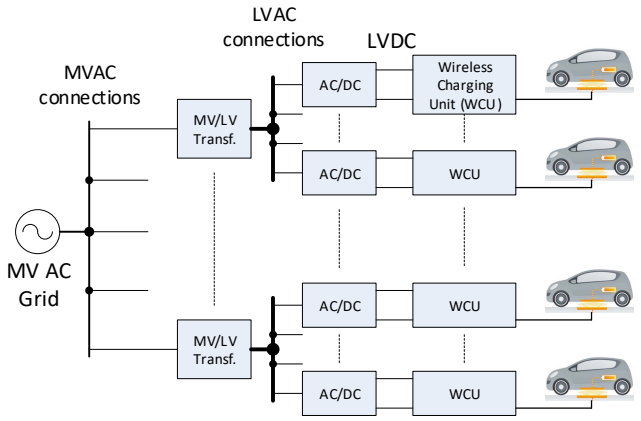

Fig. 1. Conventional power distribution topology for future large-scale parking infrastructure with wireless EV charging

expensive cabling and protection devices, together with the need for multiple MV/LV distribution transformers.

A. *Proposed modular grid interface topology*

The proposed system configuration for large-scale wireless EV charging infrastructure is presented in Fig. 2. According to the terminology introduced in [25], the grid interface is based on a double-star modular multilevel cascade converter, where each sub-module capacitor is supplying the input voltage to a wireless charging unit (WCU). Due to the high degree of freedom in defining the circulating currents that are essential for compensating unbalances in the loading, this modular multilevel converter (MMC) configuration is preferred compared to other alternative topologies of cascaded H-bridge or modular multilevel cascade converters, like the single-star or the delta-connected topologies [25]. Thus, each phase of the grid-side interface consists of two arms that are connected between the phase and the upper or lower star-point. This configuration results in a series connection of N charging units in each arm, where each WCU is supplied with a low voltage input at floating potential. The model of a charging point with a generic WCU load, supplied by a corresponding half-bridge module of the MMC topology, is presented in Fig. 3. The modular structure makes the system configuration easily scalable, and the number of charging modules connected in series within one arm can be selected according to the available MV grid and the desired capacity of the charging infrastructure.

The proposed configuration offers several advantages compared to the reference charging infrastructure layout from Fig. 1, which can be summarized as:

i. The series connection of WCUs within the arms of the MMC-based topology allows for a higher voltage rating of the grid-side interface and possibly a transformer-less connection directly to the MV grid. For large-scale charging infrastructures, this could save the costs and volume of multiple MV/LV transformers.
ii. The MMC-based topology is characterized by a low voltage THD at the ac-terminals compared to 2 level and 3 level converters, which limits the ac-side filtering requirements.

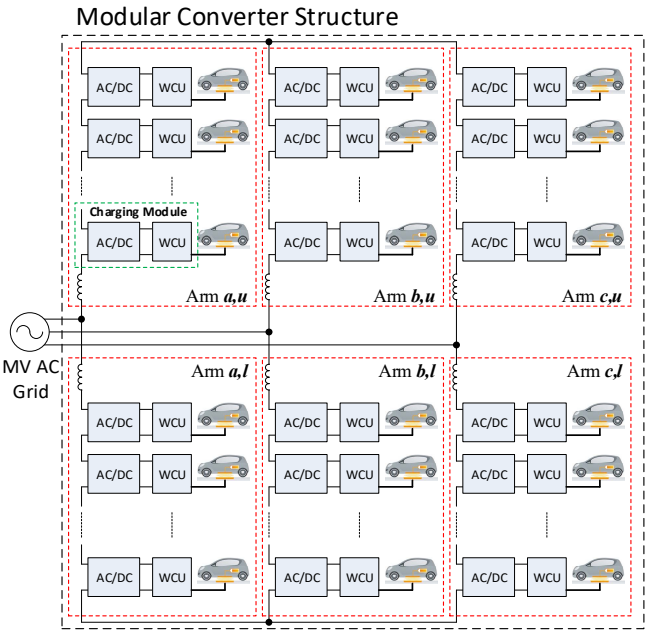

Fig. 2. Proposed topology of large-scale parking infrastructure for wireless EV charging with MMC-based grid interface

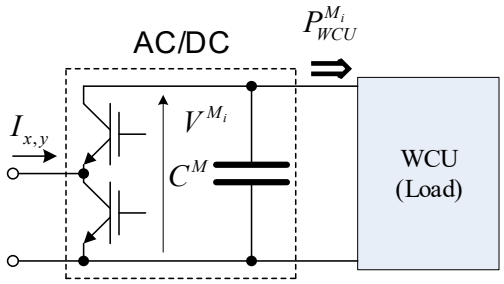

Fig. 3. Generic model of a charging module with a WCU supplied by a half-bridge based MMC module.

iii. The grid connection at higher voltage levels and the series connection of the WCUs simplifies the cabling layout and reduces the cable lengths and cross sections.

Although the proposed topology is developed specifically for large-scale charging infrastructure based on WCUs, it can be noted that the same configuration could be applicable also to conductive chargers with galvanic isolation between the power supply and the charging terminals. However, the implications on the safety requirements and the practical design of conductive chargers that could operate in the proposed topology are beyond the scope of this paper.

For illustrating the potential benefits of the proposed system configuration in terms of cabling effort, the impact on the required copper volume for internal power distribution in a charging infrastructure will be specifically analyzed in the following.

B. *Analysis of reduced cabling requirement and copper savings with the proposed topology*

The advantages of the proposed topology for reducing cable lengths and cross sections can be clarified by considering an example of a generic rectangular parking layout as shown in Fig. 4. In the considered case, the charging spots are organized

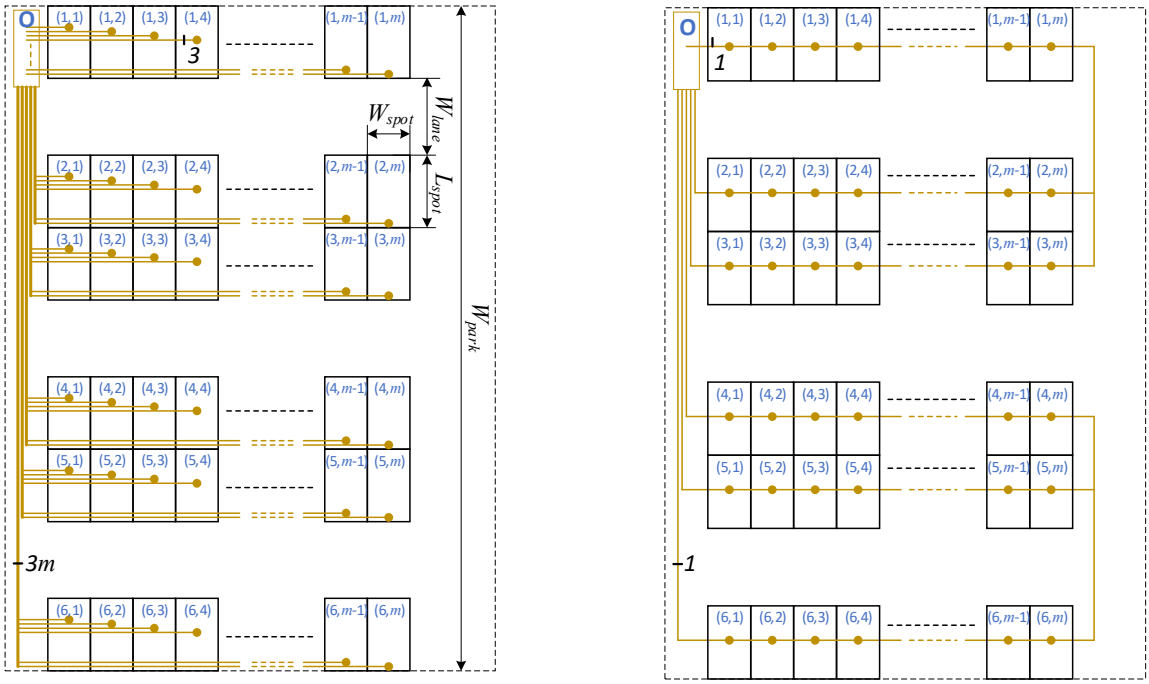

Fig. 4. Simplified cabling structure for a rectangular parking layout with 6 rows for (a) conventional charging units and (b) proposed MMC-based configuration.

in 6 rows, each containing up to m cars. The point O is the access point to the MV grid. For the conventional topology of Fig. 1, each charging spot must be connected to the LV distribution point. The necessary effort in terms of copper volume is the equivalent of having independent connections for all the spots, each rated for the charging power of a single spot. In a three-phase distribution system, the total copper cross section for each elementary connection is expressed in terms of the rated power of a single charging spot $P_{nom,chg}$ and the line-to-line rms voltage of the low-voltage distribution system $V_{LV,ll,rms}$ as:

$$S_{Cu,eq,conv} = \frac{3 \cdot I_{nom,conv}}{J_{nom}} = \frac{\sqrt{3} \cdot P_{nom,chg}}{V_{LV,ll,rms} \cdot J_{nom}}, \tag{1}$$

where J_{nom} is the allowable current density in the cables which is normally a given installation parameter.

With reference to Fig. 4(a), the total length of such elementary three-phase connections is calculated as:

$$\begin{aligned} l_{Cu,eq,conv} &\approx 6 \cdot \left((1+2+\ldots+m) \cdot W_{spot} + \frac{W_{park}}{2} \right) \\ &= 6 \cdot \left(\frac{m \cdot (m+1)}{2} \cdot W_{spot} + \frac{W_{park}}{2} \right) \end{aligned} \tag{2}$$

The required amount of copper is then proportional to the product of (1) and (2).

For the proposed layout of Fig. 4(b), a single conductor is used to series-connect all charging spots in an arm, which in this simplified scenario is assumed to coincide with a complete parking row. The resulting equivalent copper length and cross section are therefore:

$$\begin{aligned} l_{Cu,eq,MMC} &\approx 6 \cdot m \cdot W_{spot} + 4 \cdot W_{park} \\ S_{Cu,eq,MMC} &= \frac{I_{nom,MMC\,arm}}{J_{nom}} \end{aligned} \tag{3}$$

In the ideal case of perfectly balanced operation, the rated arm current of the MMC topology is expressed as:

$$I_{rat,MMC\,arm} = \frac{P_g}{2 \cdot \sqrt{3} \cdot V_{MV,ll,rms}} = \frac{\sqrt{3} \cdot m \cdot P_{nom,chg}}{V_{MV,ll,rms}} \tag{4}$$

where $V_{MV,ll,rms}$ is the line-to-line rms voltage of the MV grid.

An estimation of the copper saving related to the connection of all the charging spots to the MV access point brought about by the proposed MMC-based solution is expressed by the volume ratio:

$$k_{Cu} = \frac{vol_{Cu,MMC}}{vol_{Cu,conv}} = \frac{l_{Cu,eq,MMC} \cdot S_{Cu,eq,MMC}}{l_{Cu,eq,conv} \cdot S_{Cu,eq,conv}}, \tag{5}$$

For sufficiently long parking rows ($m \cdot W_{spot} \gg W_{park}$), the expression above tends to the very simple form:

$$k_{Cu} \approx 2 \cdot \frac{V_{LV,ll,rms}}{V_{MV,ll,rms}}, \tag{6}$$

As a numerical example, this equation implies that the proposed MMC-based topology interfaced to a 11 kV grid will require only about 7% of the copper in the cables for internal power distribution compared to a conventional LV distribution at 400 V. The gain in terms of copper savings will be even larger if higher MV levels are available. In practice, several factors may reduce the achievable gain in terms of copper usage (including reduced current density in MV conductors, need for redundancy, etc.), but this theoretical calculation indicates the potential advantages of the proposed solution.

C. *Challenges for application of the proposed topology*

A disadvantage of the proposed topology is associated with the requirement for higher insulation voltage levels resulting from the series connected configuration. Indeed, while the input capacitor voltage on each WCU can be maintained almost constant, the voltage to ground will vary continuously with the operation of the converter. Although the internal voltage levels within a module will not be influenced, these requirements should be accounted for when designing the insulation to ground for the WCUs. However, the combination of the MMC-based configuration and the wireless charging exploits the inherent benefit of IPT technology to ensure galvanic insulations from the EVs to be charged. Therefore, all parts of the system that will be exposed to the full voltage range of the MV grid are related to the sending side of the WCUs, which can possibly be integrated and encapsulated within the infrastructure. Thus, no extra design measures will be needed for the equipment on the vehicles. Indeed, the general public or the users of the vehicles will not be exposed to the voltage levels of the charging infrastructure, and the functionality for a user will be the same as for a WCU supplied by a conventional layout.

The increased complexity of the control functions required for the MMC-based topology can be considered another potential disadvantage. In the proposed configuration, each individual WCU drains power directly from a module of the MMC-based grid interface. Thus, the loading of the individual modules depends on the location and power demand of the EVs to be charged. Since it is not likely that all charging units will be in operation at the same time and delivering the same power, significant unbalances in the loading between the arms and within each arm must be expected. Such load unbalances will require additional control features compared to a conventional MMC where the cells are not individually loaded, which can result in higher circulating currents.

In general, for the proposed topology to be acceptable, the operation must be controlled so that both the interface with the grid and the interface with the chargers have the same characteristics of a conventional system:

i. Currents flowing at the point of connection to the grid should be sinusoidal and symmetrical. Their magnitude and phase angle should be regulated to match the overall active power consumption and potentially to track the reference for reactive power support to the grid.
ii. The average input dc voltage to the charging modules should be regulated to a desired value.

The following sections will discuss how the above characteristics can be achieved despite the expected internal unbalance.

III. AGGREGATED MODELLING AND POWER BALANCING REQUIREMENTS OF THE PROPOSED TOPOLOGY

Uneven distribution of the cars to be charged in the proposed topology will lead to unbalanced loading between the six arms of the converter. Therefore, compensation by control is needed to ensure balanced three phase currents and to avoid unbalances in the capacitor voltages which could possibly lead to maloperation of the converter. Since the balancing of aggregated loads in the different arms of the converter must be obtained by transferring power between the arms, the corresponding balancing requirements can be studied by considering an aggregated equivalent arm model. Thus, the averaged arm model (AAM) of MMCs [26]-[28] is expanded with an aggregated load at each equivalent arm capacitor and applied for evaluating the power balancing requirements resulting from unbalanced aggregated loading.

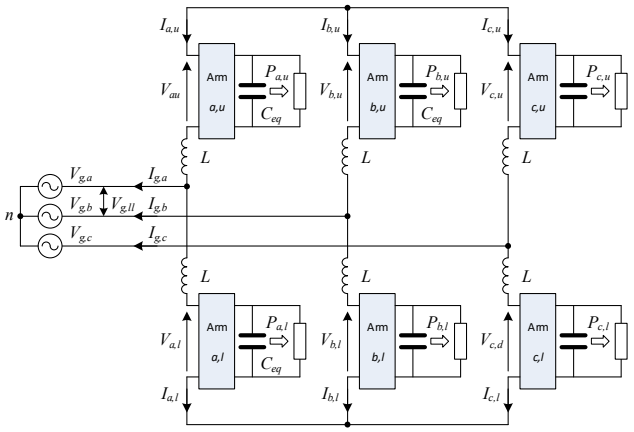

Fig. 5. Averaged Arm Model of double-star MMC converter with individually loaded arms.

A. *Modelling for analysis of power balancing*

The averaged arm representation of the studied topology is shown in Fig. 5 and serves as a reference for defining the main variables and the notation used for analysis of the system. This figure shows the main current and voltage variables, where $I_{g,abc}$ are the grid-side currents, $I_{abc,ul}$ refer to the upper and lower arm currents of each phase, $V_{g,abc}$ is the grid voltages and $V_{abc,ul}$ is the total output voltage from each arm. The total power flow in each arm can be represented as a set of aggregated loads, $P_{abc,ul}$, drawing power from each equivalent dc-side capacitor in the averaged arm model.

A per-unit representation is applied for all variables, as denoted by lower case symbols corresponding to the upper case symbols applied for physical variables in Fig. 5 and Fig. 3. The base values for the per unit system are derived from the total power rating P_B, calculated as the sum of the base power of each module ($P_B = 6\ N \cdot P^M_B$). Grid voltages are normalized to the rated peak value of the grid-side phase voltage V_B, while all currents in the system are normalized to the peak phase current calculated from the base values of power and ac voltage ($I_B = 2P_B/3V_B$).

The maximum values of the arm voltages $V_{abc,ul}$ that can be generated will be limited by the sum of the individual capacitor voltages:

$$V^{\sigma}_{x,y} = \sum_{i=1}^{N} V^{M_i}_{x,y}, \quad x \in \langle a,b,c \rangle, \quad x \in \langle u,l \rangle \tag{7}$$

According to the notation introduced in (7), the indices x and y will in the following represent the generic phase a, b, or c and the upper (u) or lower (l) arm, respectively.

For establishing a consistent per unit system, the arm voltages and the sum capacitor voltages $V^{\sigma}_{abc,ul}$ are normalized to $V^{\sigma}_{B} = 2\ V_{B}$. Individual cell dc voltages are normalized to V^{σ}_{B} / N. The voltage margin k_V is further defined as follows:

$$k_V = \frac{V^{\sigma}}{2 \cdot \hat{V}_g} = \frac{v^{\sigma}}{\hat{v}_g} \tag{8}$$

In the applied pu system, $k_V = 1$ corresponds to operating with an arm dc voltage equal to the peak-to-peak value of the phase voltage at the grid-side interface.

For analyzing the power balancing requirements, the relationship between the total per unit load and the loads of individual cells and arms must also be defined. Neglecting losses, the total per unit active power drawn from the grid can be defined as the scaled sum of all arm loads, which in turn is the scaled sum of all per unit loads on the individual modules:

$$p_g = \frac{1}{6} \sum_{\substack{x=a,b,c \\ y,u,l}} p^{\sigma}_{x,y} = \frac{1}{6} \sum_{\substack{x=a,b,c \\ y,u,l}} \left(\frac{1}{N} \sum_{i=1}^{N} p^{M_i}_{x,y} \right) \tag{9}$$

The horizontal unbalance, defined as the unbalance between the different phases, can be quantified by subtracting the average load from the load of each phase:

$$p^{\Sigma'}_{x} = p^{\Sigma}_{x} - p_g = \frac{\left(p_{x,u} + p_{x,l}\right)}{2} - p_g \tag{10}$$

The vertical unbalance, defined as the difference between the loads of upper and lower arms of each phase, is expressed as:

$$p^{\Delta}_{x} = \frac{p_{x,u} - p_{x,l}}{2} \tag{11}$$

These variables are sufficient for analyzing the requirements for balancing between the aggregated loads of the arms, while the internal balancing requirements within the individual arms will be discussed separately.

B. Balancing of aggregated arm loads

It has been demonstrated in [13], [20] how horizontal and vertical unbalance can be compensated by the introduction of a current that circulates between phases of the MMC, consisting of a dc component and a fundamental frequency component. Using phasor notation for the fundamental frequency component, the generic arm currents are given as:

$$i_{x,y}(t) = i_{x,dc} + \mathrm{Re}\left(\boldsymbol{i}_{x,y,\omega} \cdot e^{j\omega t} \right) \tag{12}$$

where the phasor is denoted by bold italic symbols. Imposing the power balance conditions and neglecting losses, the dc components of the arm currents can be related to the horizontal unbalance of the aggregated arm loads as:

$$i_{x,dc} = \frac{1}{4} \cdot \frac{p^{\Sigma'}_{x}}{v^{\sigma\Sigma}_{x}} \tag{13}$$

where $v^{\sigma\Sigma}$ is the sum component of the equivalent arm voltages defined from the per unit representation of (7) as:

$$v^{\sigma\Sigma}_{x} = \frac{v^{\sigma}_{x,u} + v^{\sigma}_{x,l}}{2} \tag{14}$$

The sum of the dc-components given by (13) for all the three phases will inherently be zero, since the studied system topology does not have any common dc terminal.

The fundamental frequency component required for compensating the vertical unbalance must fulfill the following set of linear phasor equations, defined by Kirchhoff's circuit laws applied to the topology of Fig. 5:

$$\begin{cases} \boldsymbol{i}_{x,u} - \boldsymbol{i}_{x,l} = \boldsymbol{i}_{g,x} \\ \boldsymbol{v}_{x,u} + \boldsymbol{v}_{x,l} + j \cdot x_L \cdot \left(\boldsymbol{i}_{x,u} + \boldsymbol{i}_{x,l} \right) = 0 \\ \boldsymbol{v}_{x,l} + j \cdot x_L \cdot \boldsymbol{i}_{x,l} = \boldsymbol{v}_{g,x} \\ \boldsymbol{i}_{a,u} + \boldsymbol{i}_{b,u} + \boldsymbol{i}_{c,u} = 0 \end{cases}, \tag{15}$$

Since the fundamental frequency component of the circulating current cannot transfer power between different legs, the following relationship must also hold for all three phases:

$$p^{\Sigma}_{x} = 2\left(\mathrm{Re}\left(\boldsymbol{v}_{x,u} \cdot \breve{\boldsymbol{i}}_{x,u} \right) + \mathrm{Re}\left(\boldsymbol{v}_{x,l} \cdot \breve{\boldsymbol{i}}_{x,l} \right) \right) \tag{16}$$

Solving the set of equations defined by (15) and (16), the required fundamental frequency components of each arm current can be expressed as a function of the power components defined by (9)-(11) as:

$$\begin{cases} \boldsymbol{i}_{a,u} = \frac{1}{2 \cdot \hat{v}_g} \left(-\left(p_g + p^{\Delta}_{a} \right) + j \cdot \left(q - \frac{1}{\sqrt{3}} \cdot \left(p^{\Delta}_{b} - p^{\Delta}_{c} \right) \right) \right) \\ \boldsymbol{i}_{a,l} = \frac{1}{2 \cdot \hat{v}_g} \left(\left(p_g - p^{\Delta}_{a} \right) + j \cdot \left(-q - \frac{1}{\sqrt{3}} \cdot \left(p^{\Delta}_{b} - p^{\Delta}_{c} \right) \right) \right) \\ \boldsymbol{i}_{b,u} = \frac{1}{2 \cdot \hat{v}_g} \left(-\left(p_g + p^{\Delta}_{b} \right) + j \cdot \left(q - \frac{1}{\sqrt{3}} \cdot \left(p^{\Delta}_{c} - p^{\Delta}_{a} \right) \right) \right) \cdot \boldsymbol{\alpha}^2 \\ \boldsymbol{i}_{b,l} = \frac{1}{2 \cdot \hat{v}_g} \left(\left(p_g - p^{\Delta}_{b} \right) + j \cdot \left(-q - \frac{1}{\sqrt{3}} \cdot \left(p^{\Delta}_{c} - p^{\Delta}_{a} \right) \right) \right) \cdot \boldsymbol{\alpha}^2 \\ \boldsymbol{i}_{c,u} = \frac{1}{2 \cdot \hat{v}_g} \left(-\left(p_g + p^{\Delta}_{c} \right) + j \cdot \left(q - \frac{1}{\sqrt{3}} \cdot \left(p^{\Delta}_{a} - p^{\Delta}_{b} \right) \right) \right) \cdot \boldsymbol{\alpha} \\ \boldsymbol{i}_{c,l} = \frac{1}{2 \cdot \hat{v}_g} \left(\left(p_g - p^{\Delta}_{c} \right) + j \cdot \left(-q - \frac{1}{\sqrt{3}} \cdot \left(p^{\Delta}_{a} - p^{\Delta}_{b} \right) \right) \right) \cdot \boldsymbol{\alpha} \end{cases} \tag{17}$$

where $\boldsymbol{\alpha} = e^{j\frac{2\pi}{3}}$ and $\hat{v}_g$ is the per unit amplitude of the grid voltage, assuming a balanced three phase grid.

Although the application of (13) and (17) in (12) defines the condition for balancing of the aggregated arm loads, a closed loop control strategy is needed for practical operation of the proposed topology.

IV. CONTROL SYSTEM DESIGN

The theoretical analysis of the power balancing requirements provides a basis for designing a suitable control strategy for the proposed MMC-based wireless charging infrastructure. However, a dynamic representation of the topology is also necessary for selecting appropriate control variables and feedback signals for the control system design.

A. Definition of variables suitable for control system implementation

For designing the control system, it is convenient to utilize a Σ/Δ representation of the variables, as commonly introduced for analysis of MMC-based HVDC converters [27], [29], [30].

Indeed, the Σ/Δ transformation of all variables also provide a separation of the main frequency components of the system, which simplifies the interpretation of the operational requirements and the control system implementation. The following notation and corresponding definitions for the Δ and Σ-components of the arm currents and voltages are applied:

$$i_{g,x} = i_x^{\Delta} = i_{x,u} - i_{x,l}, \qquad i_x^{\Sigma} = i_{x,u} + i_{x,l} \tag{18}$$

$$v_x^{\Delta} = \frac{1}{2}\left(v_{x,l} - v_{x,u}\right), \qquad v_x^{\Sigma} = \frac{1}{2}\left(v_{x,l} + v_{x,u}\right) \tag{19}$$

It is noted that the Δ-component of the arm voltages drives the grid-side current, while the Σ-component drives the circulating current of each phase. The insertion indices $d^{\sigma}_{x,y}$ relate the arm voltage to the sum capacitor voltage of the arm according to:

$$v_{x,y} = d^{\sigma}_{x,y} \cdot v^{\sigma}_{x,y} \tag{20}$$

with $d^{\sigma}_{x,y}$ given by:

$$d^{\sigma}_{x,y} = \frac{1}{N} \cdot \sum_{i=1}^{N} d^{M_i}_{x,y} \tag{21}$$

Furthermore, the Σ-component of the sum capacitor voltage is defined by (14), while the corresponding Δ-component is given by:

$$v_x^{\sigma\Delta} = v^{\sigma}_{x,u} - v^{\sigma}_{x,l} \tag{22}$$

It is assumed in the following that the internal balancing of the cell capacitor voltages is ensured by a sorting-algorithm, as first proposed in [31], while the insertion indices of the individual arms are calculated as [27], [29]:

$$d^{\sigma}_{x,u} = \frac{-v_x^{\Delta*} + v_x^{\Sigma*}}{v^{\sigma}_{x,u}}, \qquad d^{\sigma}_{x,l} = \frac{v_x^{\Delta*} + v_x^{\Sigma*}}{v^{\sigma}_{x,l}} \tag{23}$$

Here, * is introduced as an annotation for indicating reference signals for the Δ- and Σ-components of the arm voltages, as generated by the control system. The Δ- and Σ-components of the insertion indices can then also be defined as [29], [30]:

$$d_x^{\sigma\Delta} = d^{\sigma}_{x,u} - d^{\sigma}_{x,l}, \qquad d_x^{\sigma\Sigma} = d^{\sigma}_{x,u} + d^{\sigma}_{x,l} \tag{24}$$

Extending the expressions from [29], [30], by including the aggregated loading of the arms, the dynamic equations for the equivalent Σ and Δ capacitor voltages under aggregated arm loading can be approximated as:

$$\dot{v}_x^{\sigma\Sigma} \approx \frac{\omega_B}{4 \cdot c_{eq}} \cdot \left(d_x^{\sigma\Sigma} \cdot i_x^{\Sigma} + d_x^{\sigma\Delta} \cdot i_x^{\Delta} - \frac{p_x^{\Sigma}}{v_x^{\sigma\Sigma}} \right) \tag{25}$$

$$\dot{v}_x^{\sigma\Delta} \approx \frac{\omega_B}{4 \cdot c_{eq}} \cdot \left(d_x^{\sigma\Sigma} \cdot i_x^{\Delta} + d_x^{\sigma\Delta} \cdot i_x^{\Sigma} + \frac{p_x^{\Delta}}{v_x^{\sigma\Sigma}} \right) \tag{26}$$

where ω_B is the base angular frequency and c_{eq} is defined by:

$$c_{eq} = \frac{C^M}{N \cdot C_B}, \quad C_B = \frac{I_B}{\omega_B \cdot V_B} \tag{27}$$

The approximation in (25) and (26) results from the assumption of the voltage difference $v_x^{\sigma\Delta}$ being significantly smaller than the voltage sum $v_x^{\sigma\Sigma}$. This approximation will remain reasonable in practical operation since $v_x^{\sigma\Delta}$ will be controlled to zero. From these basic equations, control loops that fulfill the objectives defined at the end of section III.B and achieve power balance between the six arms can be designed.

B. Control of average capacitor voltages by the d-axis grid-side current reference

Assuming that all the sum arm voltages v^{σ} should be controlled to the same value, the average voltage of all arms can be represented by the zero sequence component of the voltage sum, $v^{\sigma\Sigma}z$. Based on the model in [29], it can be shown that the dynamic equation for the zero sequence voltage component of the studied topology without dc-terminals can be approximated by:

$$\dot{v}_z^{\sigma\Sigma} \approx \frac{\omega_B}{4 \cdot c_{eq}} \left(d_d^{\sigma\Delta} \cdot i_d^{\Delta} - \frac{1}{3} \cdot \sum_{x=a,b,c} \frac{p_x^{\Sigma}}{v_x^{\sigma\Sigma}} \right) \tag{28}$$

For this approximation, it is assumed that the second harmonic components of $d^{\sigma\Sigma}$ are negligible compared to the zero-sequence component and that $d_q^{\sigma\Delta}$ is very small. Thus, the *d*-axis component of the grid-side current i^{Δ} should be used for balancing the total load while regulating the average value of the equivalent arm voltages. In this paper, a PI-controller providing the d-axis current reference $i^{\Delta*}_d$ is utilized for this purpose.

C. Control of horizontal unbalance by the dc-component of the circulating current

As already defined by (13), the horizontal unbalance should be compensated by the dc-component of the circulating current. Based on (26), this can be achieved by regulating the average value of $v^{\sigma\Sigma}{}_x$ to the same level for all the three phases. Again, PI-controllers are applied for this purpose, providing the dc component of the circulating current reference, $i^{\Sigma*}{}_{dc,x}$ for each phase. These PI controllers are operating on the average value of the sum equivalent arm voltage, $\bar{v}^{\sigma\Sigma}{}_x$, which in this case is obtained from a sliding window filter. However, any other similar techniques for eliminating the ripple component in the sum of the capacitor voltages could be applied.

D. Control of vertical unbalance by the fundamental frequency component of the circulating current

From (26), it follows that the fundamental frequency component of the circulating current $i^{\Sigma}_{x,\omega}$ can be utilized for vertical balancing, as also well established for MMCs in HVDC applications [27], [32]. Calculating the Σ-component of (17) and expressing the resulting fundamental frequency circulating current in terms of positive and negative sequence components results in:

$$\begin{cases} i^{\Sigma}_{d,+\omega} = -\dfrac{1}{\hat{v}_g} \cdot \underbrace{\dfrac{p_a^{\Delta} + p_b^{\Delta} + p_c^{\Delta}}{3}}_{p_z^{\Delta}} \\ \boldsymbol{i}^{\Sigma}_{-\omega} = \overbrace{-\dfrac{1}{\hat{v}_g} \cdot \underbrace{\dfrac{2p_a^{\Delta} - \left(p_b^{\Delta} + p_c^{\Delta}\right)}{3}}_{p_{\alpha}^{\Delta}}}^{i^{\Sigma}_{d,-\omega}} + j \cdot \overbrace{-\dfrac{1}{\hat{v}_g} \cdot \underbrace{\left(\dfrac{1}{\sqrt{3}} \cdot \left(p_c^{\Delta} - p_b^{\Delta} \right) \right)}_{p_{\beta}^{\Delta}}}^{i^{\Sigma}_{q,-\omega}} \end{cases} \tag{29}$$

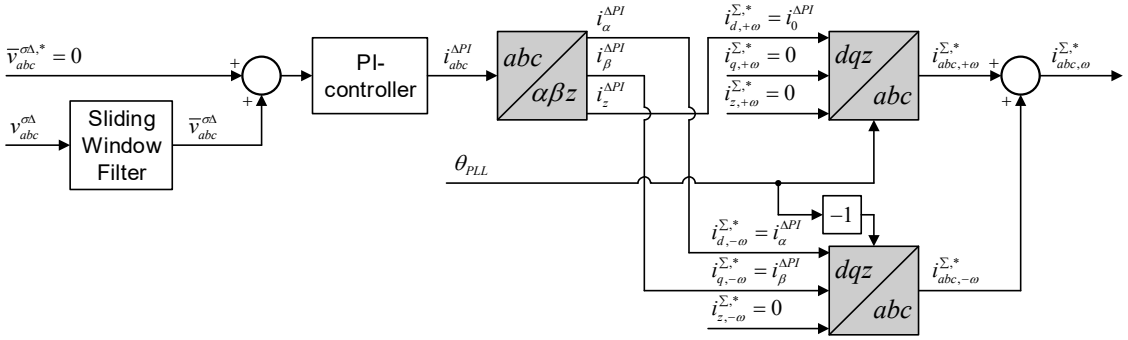

Fig. 6. Control loop for regulating the arm voltage differences to zero

This equation clearly shows that the real part (i.e. the *d*-axis component) of the positive sequence circulating current is associated with the average value (i.e. the zero-sequence component) of the vertical power unbalance. Furthermore, the real part (i.e. the *d*-axis component) of the negative sequence current component contributes to the balancing between load in phase *a* and the two other phases (i.e. the α component of the vertical power unbalance). Finally, the imaginary part (i.e. the q-axis component) of the negative sequence circulating current contributes to the balancing between phase *c* and *b* (i.e. the *β* component of the vertical power unbalance).

On basis of the dynamics defined by (26), three PI-controllers operating on the average value of the arm capacitor voltage difference, $\bar{v}^{\sigma\Delta}_{x}$, can be applied for regulating the vertical voltage unbalance to zero. The output of these PI-controllers must then be utilized according to the characteristics identified in (29). Thus, the zero-sequence component of the output from the PI-controllers of the three phases should generate the positive sequence *d*-axis current reference, $i^{\Sigma*}_{d,+\omega}$. Similarly, inspired by [33], the *α*- and *β* components of the output from the PI-controllers should provide the reference signals for the *d*- and *q*-axis component of the negative sequence fundamental frequency circulating currents, $i^{\Sigma*}_{d,-\omega}$ and $i^{\Sigma*}_{q,-\omega}$, respectively. An illustration of how the fundamental frequency reference signals for the circulating currents, $i^{\Sigma*}_{abc,\omega}$, are generated from the individual PI controllers of each phase is presented in Fig. 6. Please note that since the PI-controllers operate on the average value of the voltage difference for each phase, the *α*- and *β* components of the controller outputs will be dc-signals. Thus, the figure illustrates how the *α*- and *β* and zero-sequence components of the signals resulting from the PI-controllers can be directly utilized to define the positive and negative sequence circulating currents references in their associated synchronous reference frames.

E. Control system overview

Based on the previous discussions, a complete control strategy for operation of the proposed system configuration can be synthesized. An overview of the resulting control structure is shown in Fig. 7. In addition to the control loops already discussed, the overall control strategy includes the following functions:

i) **Grid-side current control:** The Σ/Δ representation of the currents and arm voltages according to (18) and (19) implies that the grid-side currents and the circulating currents of the MMC-based topology can be controlled independently. In this paper, a standard decoupled *dq* current control in the synchronously rotating reference frame is applied for controlling the grid-side currents, as in [30].

ii) **Grid Synchronization:** A conventional *dq*-frame Phase Locked Loop (PLL) is applied in this case for synchronizing the control system to the grid voltage. Since the PLL is designed to align the *d*-axis to the voltage vector of the grid, the *d*-axis current component determines the total active power flowing from the grid into the charging infrastructure, while the reactive power exchange with the grid is controlled by the *q*-axis current component. For simplicity, unity power factor operation with the reactive current reference $i^{\Delta*}_{q}$ set to zero is assumed in the following.

iii) **Second harmonic current reference calculation**: In the following sections, it will be shown that a second harmonic circulating current can be utilized to ensure feasibility of intra-arm balancing of the studied topology. Thus, a second harmonic current reference $i^{\Sigma*}_{x,2\omega}$ will be calculated according to the load distribution within the system.

iv) **Circulating current control**: From the previously described parts of the control system, the circulating current reference required to ensure the power balancing of the studied topology is given by three frequency components:

$$i^{\Sigma*}_{x} = i^{\Sigma*}_{dc} + i^{\Sigma*}_{\omega} + i^{\Sigma*}_{2\omega} \tag{30}$$

For simplicity, PI controllers are applied in this paper to control the circulating currents, as in [34].

v) **Arm insertion index calculation:** The insertion indices for each arm are calculated according to (23), which includes continuous compensation for the variations in the individual sum arm voltages [29], [32].

vi) **Generation of cell insertion indices**: The individual insertion indices of all modules are generated from the arm insertion indices while considering the available capacitor voltages, applying a sorting algorithm according to [31] and [35] for maintaining the capacitor voltage balance.

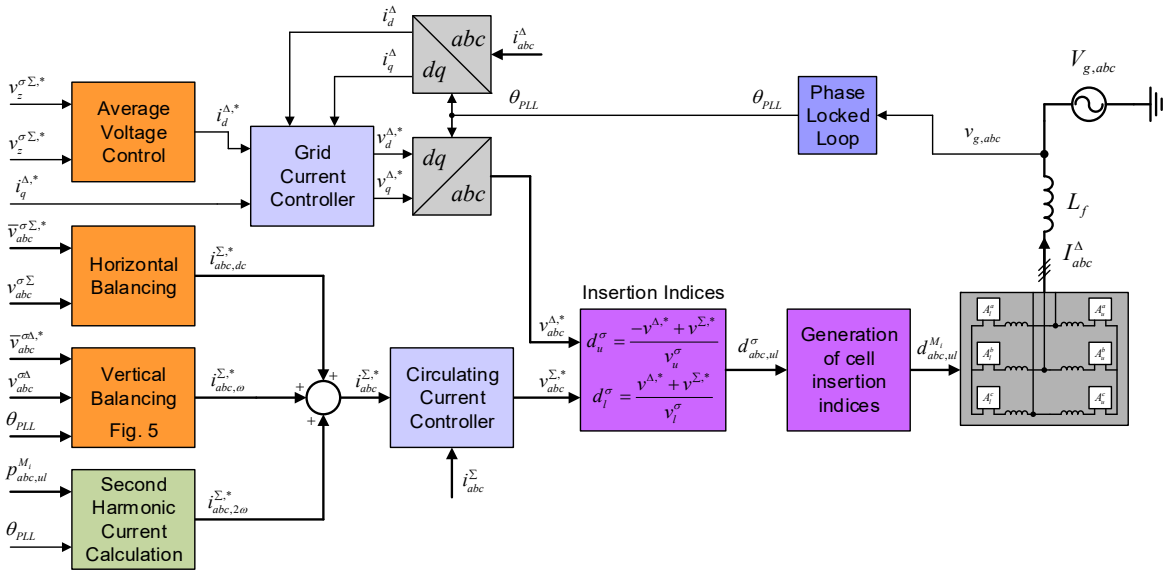

Fig. 7. Control Strategy for MMC-based transformer-less EV charging infrastructure

While the control system shown in Fig. 7 is designed for operation in balanced three-phase grids, it could be easily expanded to consider also limited level of unbalance in the grid voltages. This would mainly imply changes in the grid-side current control and the grid synchronization strategy, which are implemented in the positive sequence *dq* reference frame. Indeed, the horizontal and vertical balancing, as well as the circulating current control, are already implemented in the phase coordinates and would be inherently capable of operating under unbalanced conditions. As long as the control system would be able to keep the average capacitor voltages of the individual modules at the at the desired level, the operation of the EV-chargers would also be effectively decoupled from any small unbalances in the ac-side voltage. However, operation under severe unbalances or transient fault conditions would require a dedicated analysis of how the arm currents can be limited to safe values while complying with the requirements for the load balancing.

V. INTRA-ARM BALANCING

Once the six aggregated arms in Fig. 5 are balanced by the dc- and fundamental frequency current components given by the control loops defined in the previous section, the problem of balancing all the capacitor voltages of individual cells within each arm still needs to be addressed. Since all inserted modules of a given arm share the same current, the control of the power flow between the ac-side and the dc-side of a module can be achieved by acting on its insertion index, which is the equivalent duty cycle of the half-bridge shown in Fig. 3. In case of a load that is draining power from the dc-side of a module, the insertion index should be high when the arm current is positive and low when the arm current is negative. In most conventional MMC systems, sorting algorithms that prioritize the modules according to thee capacitor voltages are used for generating the total arm voltage [31]. Such algorithms are enough to ensure long-term balancing of the dc voltages of modules that are all nominally identical. However, theoretical limits for the intra-arm balancing capabilities emerge when modules within the same arm can have considerably different loading, as in the case of the proposed application.

A. Necessary conditions for voltage balancing within an arm

For the average voltage across the capacitance of a module over a fundamental period T to remain stable, the following charge balance equation must hold:

$$\frac{1}{T}\int_0^T d_{x,y}^{M_i}(t)\cdot I_{x,y}(t)\cdot dt = \frac{P_{x,y}^{M_i}}{V^{M_i}} \tag{31}$$

Assuming that all dc-link voltages of the cells in the arm are approximately constant and have the same value, per unit representation of the quantities in (31) leads to:

$$\frac{1}{T}\int_0^T d_{x,y}^{M_i}(t)\cdot i_{x,y}(t)\cdot dt = \frac{p_{x,y}^{M_i}}{8\cdot v_{x,y}^{\sigma}} \tag{32}$$

An ideal insertion index $\tilde{d}$ that maximizes the energy flow from ac-side to dc-side of the module is defined as:

$$\tilde{d}_{x,y}^{M_i}(t) = \begin{cases} 1 & \text{if } i_{x,y}(t) > 0 \\ 0 & \text{otherwise} \end{cases} \tag{33}$$

which implies that the module should be connected if, and only if, the arm current has a polarity that would cause charging of the capacitor. Substituting (33) into (32) results in the following necessary conditions for balancing:

$$\frac{1}{T}\int_0^T \max\left(i_{x,y}(t),0\right)\cdot dt \geq \frac{p_{x,y}^{M_i}}{8\cdot v_{x,y}^{\sigma}} \tag{34}$$

With reference to the system in Fig. 2, it is possible to find loading configurations that result in arm currents that do not fulfill (34), leading to collapse of the capacitor voltage of

some of the modules. In order to illustrate this aspect, a simple case is considered, characterized by unity power factor operation of the system ($i^{A^*}_q = 0$) and the same number of cells N_1 loaded with cell power p_{cell} on each of the six arms. The aggregated load is then the same on all arms and can be expressed as:

$$p_{arm} = \frac{N_1}{N} \cdot p_{cell} = n_1 \cdot p_{cell}, \qquad 0 \le n_1 \le 1 \tag{35}$$

Considering for instance arm *a,u*, from (17) the arm current can be expressed as:

$$i_{a,u}(t) = -\frac{n_1 \cdot p_{cell}}{2 \cdot \hat{v}_g} \cdot \cos(\omega t) \tag{36}$$

Writing the inequality (34) for the loaded cells in the arm using (36) and (35) for the arm current and the cell power, respectively, the following necessary condition for cell balancing within the arm is obtained:

$$\frac{v^{\sigma}}{\hat{v}_g} \ge \frac{\pi}{4 \cdot n_1} \quad \Rightarrow \quad n_1 \ge \frac{\pi}{4 \cdot k_V} \tag{37}$$

Thus, there is a clear relationship between the relative number of loaded cells in the arms, n_1, and the operating voltage margin k_V. For a given k_V, there is a minimum number of loaded cells below which the system cannot operate unless additional countermeasures are taken. Systems operated with higher voltage margin necessitate less loaded cells to fulfill the criterion in (34).

Although (37) is strictly valid only in case of balanced load configurations, the general remark related to more loaded arms being less critical in terms of cell-to-cell balancing is always valid, as it stems directly from (34). In fact, higher arm currents resulting from higher arm load increase the left-hand-side term of the inequality. Also, the beneficial effect of increased voltage margin can be inferred from (34), since higher cell capacitor voltages result in a reduced right-hand-side term while leaving the other side unaltered.

As already mentioned, fulfilling the set of constraints in (34) is only a necessary condition for successful balancing between cells of the same arm. This condition is also sufficient if the ideal insertion strategy from (33) can be implemented in practice for all the loaded cells, while still being able to generate the arm voltage required by the overall control system, as given by (20), (21). Whether this is possible depends on the loading configuration and on the operating voltage margin. If only few cells are loaded on a given arm, it is likely possible to select their insertion index according to (33) and still have the necessary degrees of freedom to satisfy (20). Thus, for all configurations with relatively few heavily loaded cells, fulfilling (34) will be equivalent to ensuring balanced operation, provided proper selection of insertion indices. On the other hand, if most cells in the arm are heavily loaded, the arm current will most likely be high enough that (34) will be satisfied with considerable margin, making the constraints on the insertion indices less stringent.

There may, however, be intermediate loading configurations where the sole fulfillment of (34) is not sufficient. Operating with relatively high voltage margin is a safe way of avoiding such situations, since high k_V not only enhances the instantaneous power flow between ac and dc side of the cell for the same arm current, but also increases the degree of freedom in the process of selecting the individual insertion indices for generating the required arm voltage.

As a further measure to ensure that the necessary conditions defined by (34) are also sufficient to ensure balanced operation, a safety margin k_m can be included in the evaluation of the charge balance criterion that takes into account other system non-idealities like unmodeled losses, unavoidable variations of the cell capacitor voltages, delays in the process that synthesizes the insertion indices, etc. The conditions that should be fulfilled can then be generalized as:

$$\frac{1}{T}\int_0^T \max\left(i_{x,y}(t), 0\right) \cdot dt \ge k_m \cdot \frac{p^{M_i}_{x,y}}{8 \cdot v^{\sigma}_{x,y}}, \qquad k_m \ge 1 \tag{38}$$

B. Increasing intra-arm balancing capability by circulating 2nd harmonic current injection

When the loading configuration is such that the conditions in (34), or the generalized form in (38), are not satisfied with the arm currents consisting only of the dc component from (13) and the fundamental frequency component from (17), the system will not have inherent intra-arm balancing capability. Thus, additional circulating currents must be deliberately introduced to maintain controllability of all module voltages.

One way to enhance the balancing capabilities of the system without interfering with the active power balance between the grid and the aggregated arm loads is to add an even order harmonic component to the circulating current. Considering a 2nd order harmonic injection, the generic arm current takes the form:

$$i_{x,y}(t) = i_{x,dc} + \mathrm{Re}\left(\boldsymbol{i}_{x,y,\omega} \cdot e^{j\omega t}\right) + \mathrm{Re}\left(\boldsymbol{i}_{x,2\omega} \cdot e^{j2\omega t}\right), \tag{39}$$

with the circulating current constraint of the 2nd harmonic component expressed as:

$$\boldsymbol{i}_{a,2\omega} + \boldsymbol{i}_{b,2\omega} + \boldsymbol{i}_{c,2\omega} = 0 \tag{40}$$

Since the added circulating current contributes to losses and increases the stress on the components, it is necessary to find the minimum possible injection that satisfies the balancing criteria of (38).

The simplest example of unbalanced arm loading for the proposed topology is if a single car requires charging in a very large parking infrastructure. In this case, the total power absorbed from the grid will be negligible and the arm current would only contain the injected 2nd harmonic component needed to balance the capacitor voltages of the arm. The condition (38) is then explicitly calculated as:

$$i_{2\omega} \ge \frac{\pi}{8 \cdot v^{\sigma}} \approx \frac{0.39}{v^{\sigma}} \tag{41}$$

This equation, although derived for a very special loading condition, carries important information about the expected order of magnitude of required circulating current and about the fact that operation with higher voltage margin leads to reduced circulating current requirements.

C. General method for calculation of 2nd harmonic current requirements

The problem of determining the minimum required 2nd harmonic circulating current for ensuring feasible operation of the system can be formulated as a constrained optimization problem. Defining the minimum required current as the one that minimizes ohmic losses in the converter, the objective function to be minimized takes the form:

$$\mathrm{f}(\mathbf{x}) = \sum_{\substack{x=a,b,c \\ y=u,l}} \int_0^T {i_{x,y}}^2 (\mathbf{p},\mathbf{x},t)\cdot dt \tag{42}$$

The arm currents are expressed in the generic form of (39), taking into account (13), (17), and are therefore a function of the aggregated loading configuration:

$$\mathbf{p} = \begin{bmatrix} p_{a,u} & p_{a,l} & p_{b,u} & p_{b,l} & p_{c,u} & p_{c,l} \end{bmatrix} \tag{43}$$

The optimization variables are the real and imaginary components of the 2nd harmonic circulating current phasors. Due to the relationship in (40), only four of the six components are independent. A feasible set of independent optimization variables is:

$$\mathbf{x} = \begin{bmatrix} i_{a,\mathrm{Re}} & i_{a,\mathrm{Im}} & i_{b,\mathrm{Re}} & i_{b,\mathrm{Im}} \end{bmatrix} \tag{44}$$

The problem is constrained by the $6N$ inequalities according to (38), expressing the necessary condition for stable system operation. However, since the current is shared by all modules in the arm, only six of those constraints need to be considered, related to the cell in the arm having the highest load, thus greatly simplifying the problem. The six constraints take the form:

$$\frac{1}{T}\int_0^T \max\left(i_{x,y}(t),0\right)\cdot dt \geq k_m \cdot \frac{\max\limits_{i=1,\ldots,N}\left(p_{x,y}^{M_i}\right)}{8\cdot v_{x,y}^{\sigma}}, \qquad \begin{matrix} x\in(a,b,c) \\ y\in(u,l) \end{matrix} \tag{45}$$

To assess the impact of the necessary 2nd harmonic injection on system performance, the optimization problem described above can been solved for many random unbalanced load configurations. The random process consists in generating uniformly distributed numbers in the range (0,1) for the aggregated load on the six arms $p_{x,y}$. For ensuring that worst-case scenarios are included, individual module loads on each arm are assigned so that at least one module per arm is loaded at its rated power:

$$p_{x,y}^{M_i} = \begin{cases} 1.0 & if\ N\cdot p_{x,y} < i \\ 0.0 & otherwise \end{cases} \qquad i = 1,\ldots,N \tag{46}$$

Note that with the load configurations in (46), the following condition is satisfied:

$$\max_{i=1,\ldots,N}\left(p_{x,y}^{M_i}\right) = 1.0 \tag{47}$$

corresponding to the worst-case for the constraints in (45).

The results of the calculation for 1000 random configurations are shown in Fig. 8 and Fig. 9, for a voltage margin k_V = 1.3. Fig. 8 shows the minimum required 2nd harmonic circulating current, in terms of the average and the worst-case rms values of the three legs. In general, these two

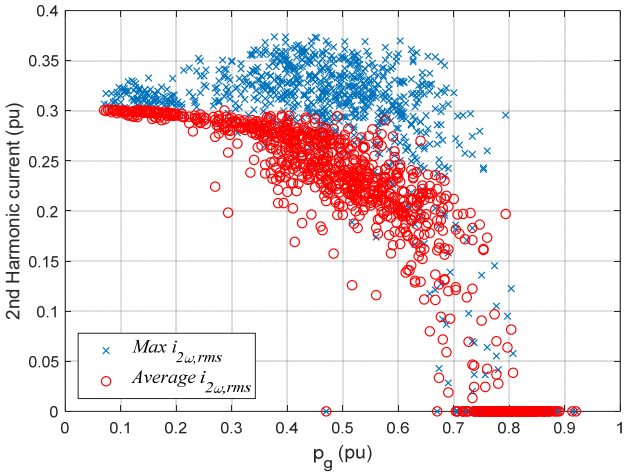

Fig. 8. Necessary 2nd harmonic circulating current for 1000 random loading configurations; k_v=1.3, k_m=1.0

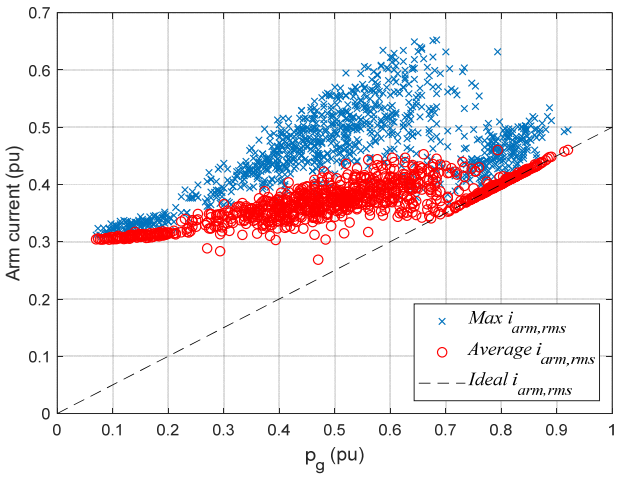

Fig. 9. Calculated rms values of arm current including 2nd harmonic for 1000 random loading configurations; k_v=1.3, k_m=1.0

quantities are different, since the load configuration on the legs impose different requirements and the optimization algorithm allows for an unbalanced 2nd harmonic component, as long as (40) is satisfied. As expected, there is a threshold for the average load above which 2nd harmonic injection is no longer required regardless of the load configuration.

Fig. 9 shows the rms of the calculated arm currents, including the injected 2nd harmonic. The worst-case over the six arms is shown, along with the average value. Moreover, the ideal arm current level corresponding to a load uniformly distributed among all the cells in the system is included for reference. An important result is that while the average of the six rms arm currents is always lower than the ideal rated arm current of 0.5 pu, there exist loading conditions leading to individual arm currents exceeding the rated value. This implies that both cabling and switching devices used for the implementation of the MMC-based parking topology of Fig. 2 would need to be overrated compared to a conventional MMC topology designed for the same rated power and operated with the same voltage margin.

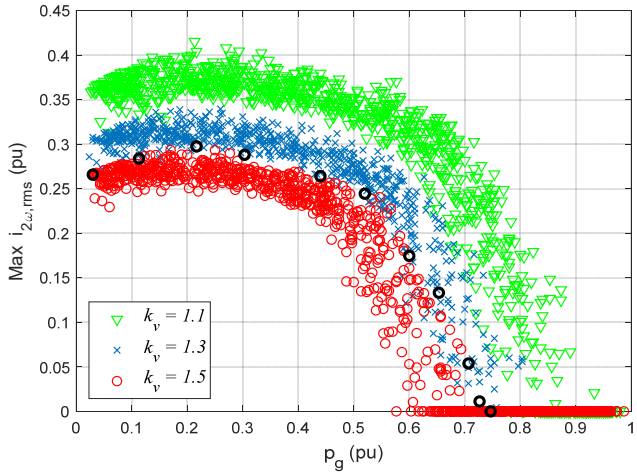

Fig. 10. Necessary 2nd harmonic current in case of limited unbalance (±20% k_m=1.0) for different operating voltage margin. Black circles correspond to the operating points in Table II.

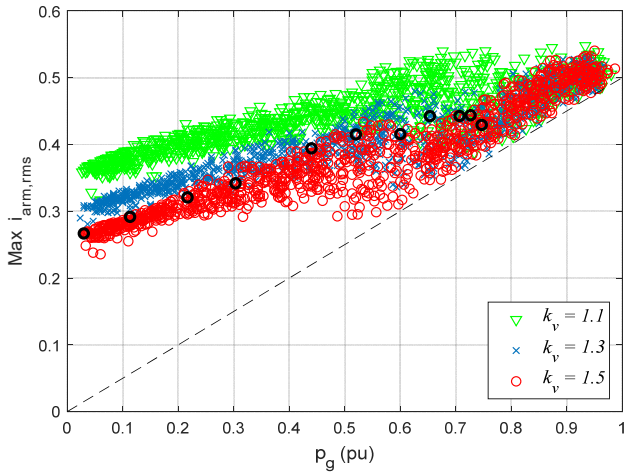

Fig. 11. Maximum total arm current in case of limited unbalance resulting from calculation of rms arm currents including the 2nd harmonic component for 1000 random loading configurations; k_m=1.0 Black circles correspond to the operating points in Table II.

Overrating the installation has serious implications in terms of cost and may prevent the acceptance of the proposed topology. The problem can be mitigated by increasing the operating voltage margin and/or limiting the maximum level of unbalance. In the proposed parking application, the latter can be achieved by implementing dedicated parking and charging management strategies as discussed in [36].

Fig. 10 and Fig. 11 show the effect of k_V and of a limited unbalance range on the calculated 2nd harmonic and total arm currents, respectively. In the figures, 1000 random loading configurations are selected so that each of the aggregated arm loads satisfies the following condition for limited unbalance:

$$\max\left(p_g - 0.2,\quad 0\right) \le p_{x,y} \le \min\left(p_g + 0.2,\quad 0\right) \qquad (48)$$

The effect of increasing k_V is evident in Fig. 10. Higher voltage margin results in reduced need for 2nd harmonic circulating current for all load configurations. Increased voltage margin also lowers the load threshold above which injection of a 2nd harmonic current is no longer required. Fig. 11 shows that the combined effect of higher voltage margin and limited load unbalance can result in worst-case arm current that does not significantly exceed what would be required for a conventional MMC having the same rated power. However, it must be noted that, for a fixed number of modules, increasing k_V causes increased voltage stress on devices and cables. If devices and/or cables with higher voltage ratings must be employed to increase k_V, this will lead to a trade-off between the advantage of reduced circulating current and the consequences of increased operating voltage.

VI. EFFECT OF LOAD UNBALANCE ON CONDUCTION LOSSES

The circulating current needed for operation under unbalanced loading conditions will inevitably cause additional system losses. Indeed, ohmic losses in the cables and conduction losses in the cells will increase by a factor that is proportional to the squared rms of the current flowing in each of the arms. Thus, for investigating the relative increase of losses due circulating currents, the following normalized loss quantity can be defined:

$$p_{loss,norm} = \frac{2}{3} \cdot \sum_{\substack{x=a,b,c \\ y=u,l}} i_{x,y,rms}^2 \qquad (49)$$

This quantity represents the ohmic losses in a given operating condition, relative to the losses incurred at rated charging power and zero unbalance, when $i_{x,y,rms} = 0.5$.

To simplify the analysis, it is assumed that all the vehicles served at a given time are charging at a fixed power level of 1.0 pu. Thus, the total charging power in pu, p_g, is directly proportional to the number of charging cars n_{cars}:

$$p_g = \frac{n_{cars}}{6 \cdot N} \qquad (50)$$

For a given number of charging EVs, their distribution within the parking lot will determine the level of unbalance and consequently the operating losses. Therefore, in probabilistic terms, the expected value of the conduction losses at a given power level can be derived as the average of the losses over all possible configurations, weighted according to the relative frequency of occurrence. A Monte Carlo analysis has been carried out for the generation of 1000 parking configurations at each power level, under the assumption of equal probability of occupancy for all parking spots. Two sets of simulations are performed, one without imposing any a-priori restriction on the unbalance (i. e. Δp_{max} =1) and one where only configurations satisfying the unbalance limitation in (48) are allowed (i. e. Δp_{max} = .2). The results from this analysis are presented in Fig. 12 in comparison to the conduction losses of an MMC with ideal balanced loading (green dashed curve).

The two solid curves in Fig. 12 clearly show that the expected average losses without (blue) and with (red) a constraint on the power unbalance, are essentially independent from the allowed maximum unbalance at all power levels. This can be explained by recognizing that configurations with

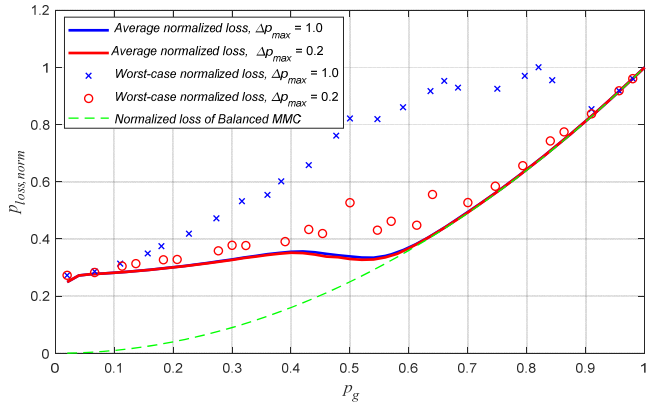

Fig. 12. Average normalized system loss as function of total charging power for different maximum allowed unbalance.

a rather small unbalance are far more likely than the ones with an extreme unbalance. The system is shown to operate with average losses comparable to a perfectly balanced MMC converter when the charging power exceeds about 0.5 pu. Losses due to the 2nd harmonic circulation become dominant at lower power levels and they can be reduced only by lowering the charging power of each vehicle, as stated by (45). This confirms that the proposed topology is well-suited for applications where a high average occupancy is expected.

The normalized losses corresponding to the worst-case configuration at several power levels are also reported in the figure. The effect of limiting the unbalance is very visible, as the worst-case losses become much lower. This corresponds to what can be interpreted from a comparison of the results in Fig. 9 and Fig. 11. However, the worst-case conditions with respect to the required circulating currents could be avoided by applying a scheduling algorithm for the EV parking, as discussed in [36].

Independently of any limitations of the unbalance, the increase of the average losses at low loading is limited to less than about 1/3rd of the conduction losses at full load. Since the unlikely cases of extreme unbalances at low load will not cause total currents or losses exceeding the values at rated load, the only consequence of such rare operating conditions will be the limited additional losses. It is also worth noting that the worst-case scenario with unlimited unbalance did not actually present itself in the Monte Carlo analysis, due to its extremely low probability.

VII. SIMULATION RESULTS

The modular charging system of Fig. 2, with parameters reported in Table I has been modeled and simulated using Matlab-Simulink. For the simulations, all modules are explicitly represented with their individual loads and a switching function-based representation of the total arm voltages.

The cases indicated with black circles in Fig. 10 and Fig. 11, with operating conditions specified in Table II, are simulated in order to verify the validity of the necessary condition for balancing and to evaluate the magnitude of the voltage margin needed to ensure that such condition is also

TABLE I – PARAMETERS OF SIMULATED MODULAR CHARGING SYSTEM

System data	
Total installed charging power, P_{nom}	3.3 MW
Nominal line-to-line grid voltage, $V_{g,nom}$	11 kV
Number of charging slots	300 (6 x 50)
MMC general data	
Number of modules per arm, N	50
Nominal arm dc voltage V^{σ}_{nom}	27 kV
Operating voltage margin k_V	1.5
MMC cell data	
Nominal load for each module, P^{M}_{nom}	11 kW
Nominal module voltage, V^{M}_{nom}	540 V
Module capacitance, C^{M}	3.4 mF

TABLE II – SIMULATED LOAD CONFIGURATIONS WITH RESULTING SAFETY MARGIN FOR CALCULATION OF 2ND HARMONIC CIRCULATION

Case number	p_{tot}	Number of loaded cells [au, ad, bu, bd, cu, cd]	Calculated $\max_{a,b,c}(i_{x,2\omega})$	Required margin k_m	Resulting $\max_{a,b,c}(i_{x,2\omega})$
1	0.03	[0, 2, 0, 6, 0, 1]	0.27	**1.01**	0.27
2	0.11	[5, 11, 2, 15, 1, 0]	0.28	**1.07**	0.30
3	0.22	[17, 19, 2, 1, 16, 10]	0.30	**1.14**	0.33
4	0.30	[14, 16, 24, 23, 10, 4]	0.29	**1.15**	0.33
5	0.44	[29, 24, 10, 24, 19, 26]	0.26	**1.06**	0.28
6	0.52	[14, 29, 23, 32, 26, 32]	0.24	**1.06**	0.28
7	0.60	[22, 30, 39, 34, 20, 35]	0.17	**1.02**	0.19
8	0.65	[42, 34, 30, 25, 42, 23]	0.13	**1.06**	0.17
9	0.71	[42, 42, 24, 41, 27, 36]	0.05	**1.07**	0.12
10	0.73	[34, 38, 39, 43, 24, 40]	0.01	**1.02**	0.05
11	0.75	[42, 36, 30, 41, 36, 39]	0	**1.00**	1

sufficient. The cases are labeled with increasing numbers (1 to 11) according to the related aggregated load power (left to right in the figures). Each load configuration is simulated with a 2nd harmonic injection calculated according to the optimization procedure of section V. with different values of safety margin k_m ranging from 0.95 to 1.2. The minimum value of k_m resulting in stable operation is reported in Table II, along with the corresponding value of 2nd harmonic injection.

A worst-case safety margin of 1.15 is needed for some rather unbalanced loading configurations with average load in the range of 0.2 to 0.4. As expected, k_m resulting in stable balancing is always bigger than or equal to one, demonstrating the validity of the necessary conditions (34).

The voltage and current waveforms related to Case 4 in the table are shown in Fig. 13 and Fig. 14, representing the worst-case of required k_m and also the highest required 2nd harmonic current among all the simulated configurations. In steady state, balanced grid currents with very low distortion and unity power factor are achieved despite the unbalanced load. The arm currents, on the other hand, are all different and contain additional dc- as well as 2nd harmonic components that are necessary for the power balancing process. Voltages of all 300 cells are stable and remain within a +/-10% window around the nominal value. Twelve different sets of waveforms are recorded for the dc voltage of the cells, corresponding to the loaded and unloaded elements in each of the six arms. Within

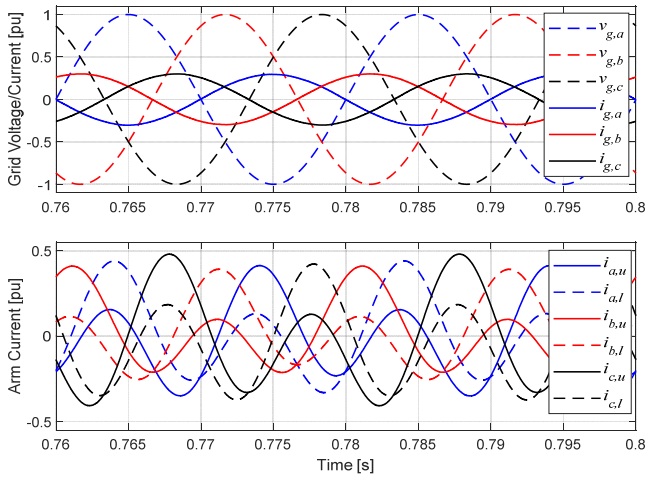

Fig. 13. Simulation of case number 4 in Table II, with 2nd harmonic injection calculated with k_m = 1.15, corresponding to the minimum value resulting in stable operation

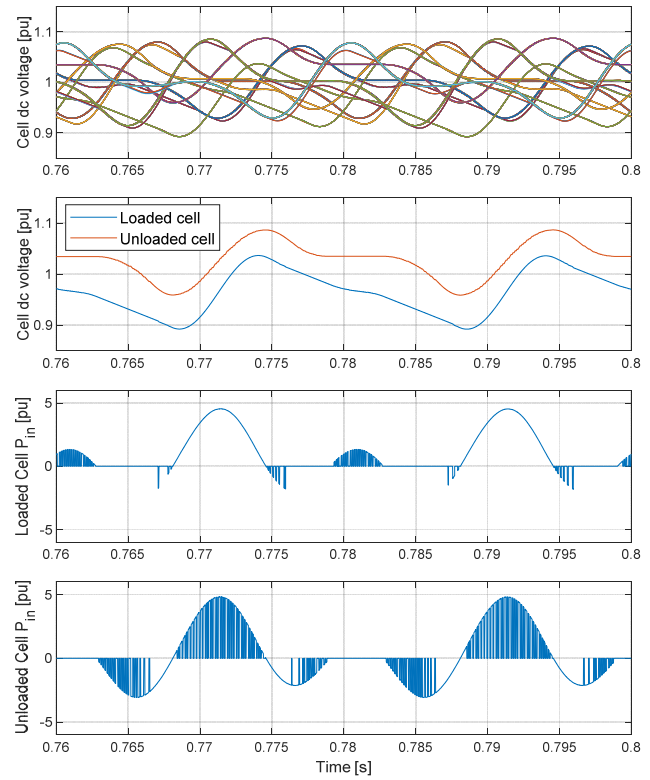

Fig. 14. Simulation of case number 4 in Table II, with 2nd harmonic injection calculated with k_m = 1.15, corresponding to the minimum value resulting in stable operation. From top to bottom: 1 – dc voltages of all the 300 modules in the system; 2 - dc voltage of one loaded module and one unloaded module in arm *b,l*; 3 – power flow from ac to dc side of a loaded module in arm *b,l*; 4 - power flow from ac to dc side of an unloaded module in arm *b,l*.

each of these sets, cells are practically indistinguishable, due to the high frequency sorting process. It is noted that the simple voltage-based sorting algorithm in use causes the average value of the dc voltages for the loaded and unloaded cells to differ slightly, although they remain stable. This deviation is one reason for the need of a safety margin in the calculation of the required harmonic injection. As expected, the loaded cells operate with an insertion index that very closely approximates the ideal expression in (33), proving the effectiveness of the sorting algorithm and also showing that the system is operating close to its theoretical limit.

TABLE III – PARAMETERS OF EXPERIMENTAL SETUP

System data	
Total installed charging power, P_{nom}	24.5 kW
Nominal line-to-line grid voltage, $V_{g,nom}$	200 V rms
Number of charging spots	72 (6 x 12)
MMC general data	
Number of modules per arm, N	12
Nominal arm dc voltage V^{σ}_{nom}	480 V
Operating voltage margin k_V	1.5
MMC cell data	
Nominal load for each module, $P^{M,nom}$	340 W
Nominal module voltage, $V^{M,nom}$	40 V
Module capacitance, C_M	15 mF

VIII. EXPERIMENTAL RESULTS

A. Laboratory setup

The proposed control approach has been validated on an experimental setup consisting of a custom-made MMC with 12 modules per arm and an external controllable load for each cell. The MMC prototype is designed to operate with ac voltage up to 400 V and dc voltage up to 700 V [38]. The individual modules can operate with dc voltage up to 80V and MOSFETs are used as switching devices. Each module is connected to a controllable switched resistor at floating potential. The voltage levels used in the experiments are indicated in Table III and have been chosen to achieve the same voltage margin that was assumed for the large-scale parking infrastructure simulated in section VI.

The main control loops of the MMC and the control of the loads are implemented on an OPAL-RT OP5600 real-time simulation platform used for rapid prototyping of the control system. As discussed for the control system design, the dc and fundamental frequency components of the circulating currents are responsible for the horizontal and vertical balancing, respectively. The references for these components are generated by the control system from Fig. 7. The 2nd harmonic circulating current is introduced to facilitate the intra-arm balancing. The references for the 2nd harmonic injection have been precalculated offline based on the intended load power distribution. An online implementation of the algorithm for identifying optimal reference values is assumed feasible but details on a real-time implementation is considered beyond the scope of this paper. The modulation of each arm and the processing of the individual cell voltage measurements are handled by a distributed control system based on a FPGAs as presented in [37], [38]. The parameters of the experimental setup is reported together with the power and voltage levels given in Table III, while a picture of the MMC-based converter unit with the individual cell loads is shown in Fig. 15. Further images from the laboratory setup are also included as a multimedia attachment of the paper.

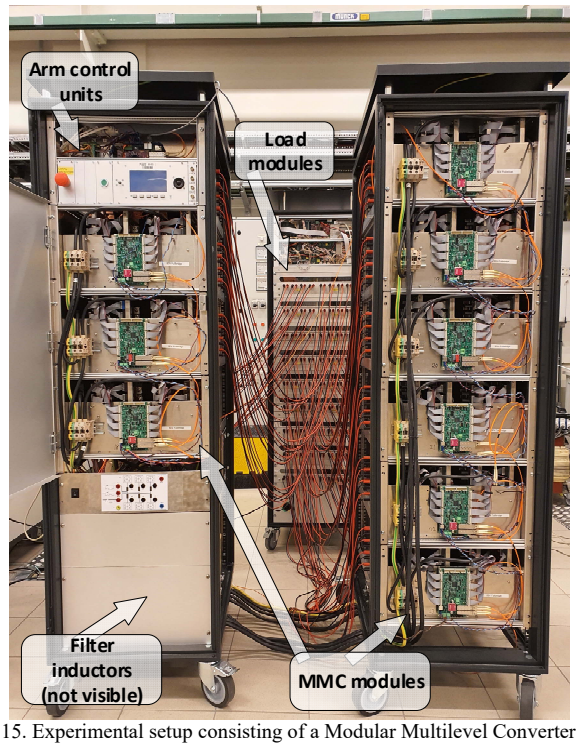

Fig. 15. Experimental setup consisting of a Modular Multilevel Converter with 12 modules per arm (the two cabinets in the front), and individual controllable loads connected to each cell capacitor (cabinet in the back).

B. Steady state operation under different loading scenarios

Four loading cases have been tested to highlight the capabilities of the proposed configuration in handling load unbalances. Specification of the loading conditions for each case are reported in Table IV. The amplitude of the harmonic components of the current measured in each arm is also indicated for reference. These components are calculated offline by postprocessing the experimentally measured currents with a conventional FFT algorithm.

Case 1 - Load unbalance between the arms without intra-arm unbalance. This case aims at verifying the vertical and horizontal balancing with a dc and a fundamental frequency component in the circulating current. The load duty cycle is identical within each arm but different between the arms. Results are presented in Fig. 16. Since no intra-arm unbalance is present, no second harmonic needs to be injected in the circulating current, as can be seen from the shape of the arm currents. The cell voltages are very well balanced, although a noticeable fluctuation appears due to the circulating current that is needed for load balancing.

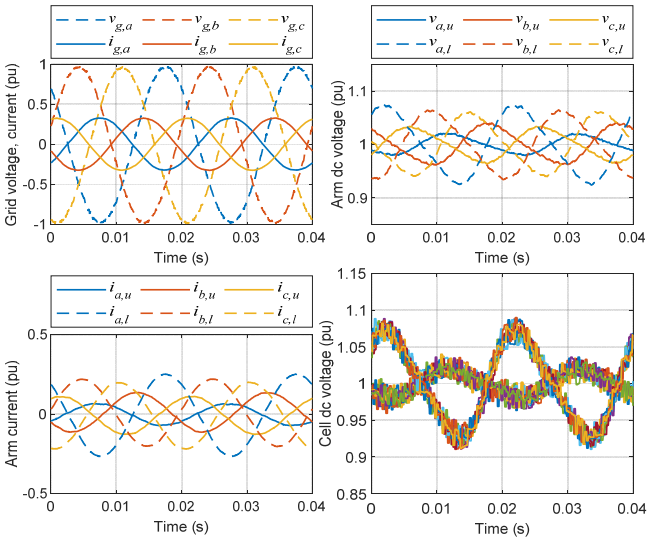

Fig. 16. Experimental results for case I.

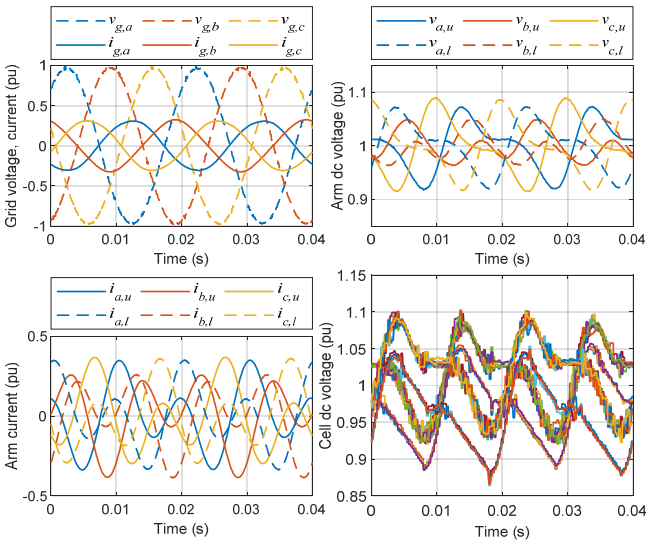

Fig. 17. Experimental results for case II.

Case 2 – Intra-arm unbalance without load unbalance between the arms. This case, with results plotted in Fig. 17,

TABLE IV –LOAD CONFIGURATIONS AND DETECTED HARMONIC COMPONENTS IN THE ARM CURRENTS

Case number	Total power [pu]	Load configuration [*a, b, c*] (number of active cells x cell power in pu 4x1&8x0 means 4 cells at 1 pu and 8 at 0 pu)		Arm currents harmonic components [pu]								
				Phase a			Phase b			Phase c		
				dc	1st	2nd	dc	1st	2nd	dc	1st	2nd
1	0.33	u	[12x0.1,12x0.3, 12x0.2]	-0.005	0.065	0	0.01	0.12	0	-0.005	0.115	0
		l	[12x0.5,12x 0.5, 12x0.4]	-0.005	0.25	0	0.01	0.205	0	-0.005	0.20	0
2	0.33	u	[4x1&8x0, 4x1&8x0, 4x1&8x0]	0	0.15	0.22	0	0.15	0.22	0	0.15	0.22
		l	[4x1&8x0, 4x1&8x0, 4x1&8x0]	0	0.15	0.22	0	0.15	0.22	0	0.15	0.22
3	0.33	u	[4x1&8x0, 6x1&6x0, 3x1&9x0]	0	0.16	0.23	0.025	0.16	0.18	-0.025	0.20	0.28
		l	[4x1&8x0,6x1&6x0, 1x1&11x0]	0	0.16	0.23	0.025	0.16	0.18	-0.025	0.12	0.28
4	0.58	u	[7x1&5x0, 9x1&3x0, 6x1&6x0]	0	0.36	0	0.025	0.36	0	-0.025	0.40	0
		l	[7x1&5x0, 9x1&3x0, 4x1&8x0]	0	0.36	0	0.025	0.36	0	-0.025	0.32	0

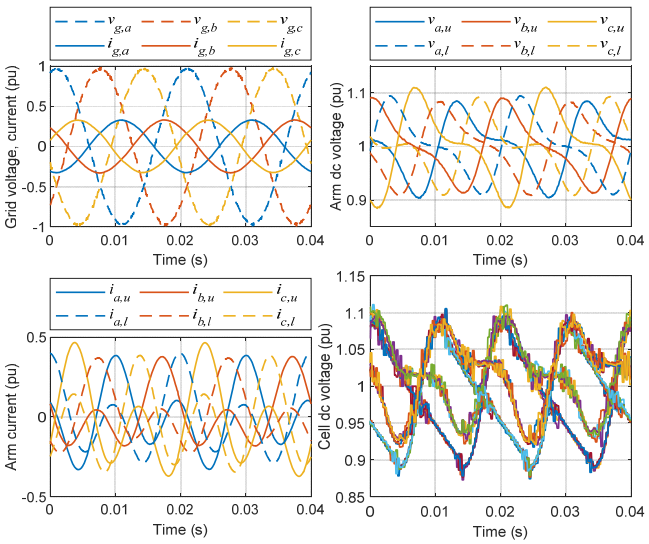

Fig. 18. Experimental results for case III.

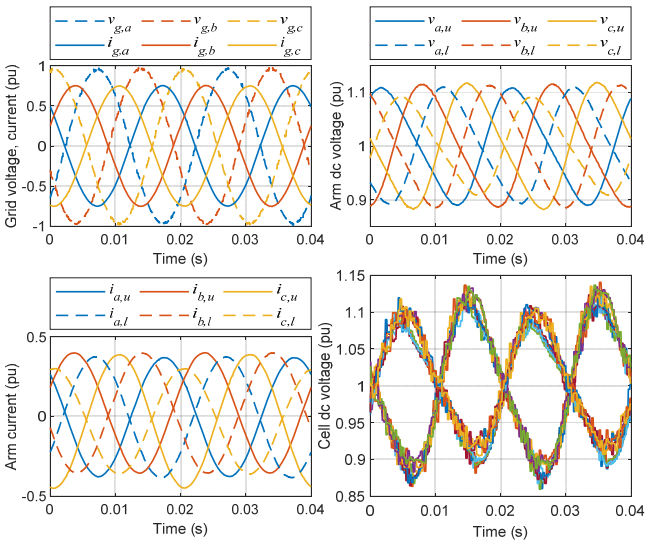

Fig. 19. Experimental results for case IV.

verifies the capabilities for compensating intra arm unbalances achieved by addition of a 2nd harmonic component in the circulating current. All arms are loaded equally but the cells within each arm are operated at different duty cycles. As can be interpreted from Fig. 17, no dc or fundamental frequency component of the circulating current is necessary. This can also be seen from the harmonic analysis in Table IV, noting that the fundamental component is the same an all arms. The cell voltages are stable, indicating a correct implementation of the balancing principle. However, the loaded cells can be clearly identified from their lower average voltage compared to the unloaded ones. This behavior is consistent with the results from the numerical simulations and is associated to the inherent operating principle of the sorting algorithm. The voltage difference between loaded and unloaded cells is reduced if higher circulating current is used, compared to the absolute minimum required amplitude that was used in the

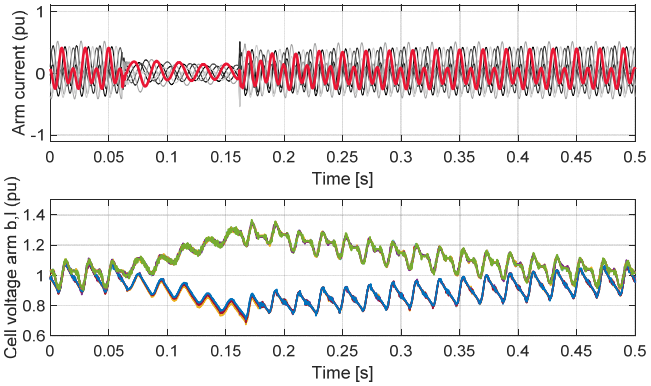

Fig. 20. Experimental results when the 2nd harmonic current injection is disabled and re-enables during operation with load as in case 3 of Table IV

experiment. The grid voltages and current appear with low harmonic distortion confirming the correct operation of the modulation algorithm in compensating unbalances and fluctuations in the individual cell voltages.

Case 3 - Load unbalance between the arms and intra arm unbalance at low grid loading. This case combines the two type of unbalances with result displayed in Fig. 18. The loading condition is a scaled-down replication of the one simulated in section VI (case 4 in Table II). In this case, a combination of dc, first harmonic and second harmonic components of the circulating current is required to balance the cell voltages, as confirmed by the waveforms and by the harmonic analysis in Table IV. The cell voltages are bounded and stable, confirming the validity of the control approach and the compatibility of the two balancing mechanisms. Due to the minimum amount of 2nd harmonic injection, the loaded cells can be still easily identified by their lower average voltage but the differences in individual cell voltages within the arms are compensated by the modulation and do not translate into harmonics in the grid current.

Case - 4 Load unbalance between the arms and intra arm unbalance at high grid loading. This case is derived from the previous case but with higher loading of the arms. Results are presented in Fig. 19. The higher arm currents associated to the loading conditions allow the intra-arm balancing without second harmonic injection as predicted by the theoretical and numerical analysis. The arm currents clearly indicate the presence of a fundamental frequency component and a modest dc current. The cell voltages are stable and bounded and the difference in average voltage between loaded and unloaded cells is rather small. This is because the arm currents in these conditions are above the minimum level necessary for intra-arm balancing, even without 2nd harmonic injection.

C. Validation of the balancing effect of the 2nd harmonic injection

As already mentioned, the fundamental frequency and dc components of the circulating currents may not be sufficient to ensure balancing capability of the capacitor voltages in presence of intra arm unbalances. The effect of the calculated requirement for 2nd harmonic injection has been validated experimentally with results shown in Fig. 20. In this case, the

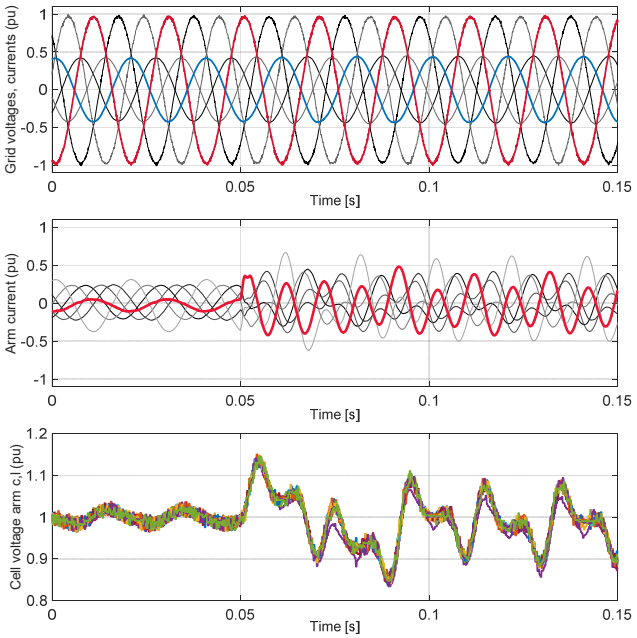

Fig. 21. Experimental results for a load step resulting in transition from no arm unbalance to significant intra-arm unbalance.

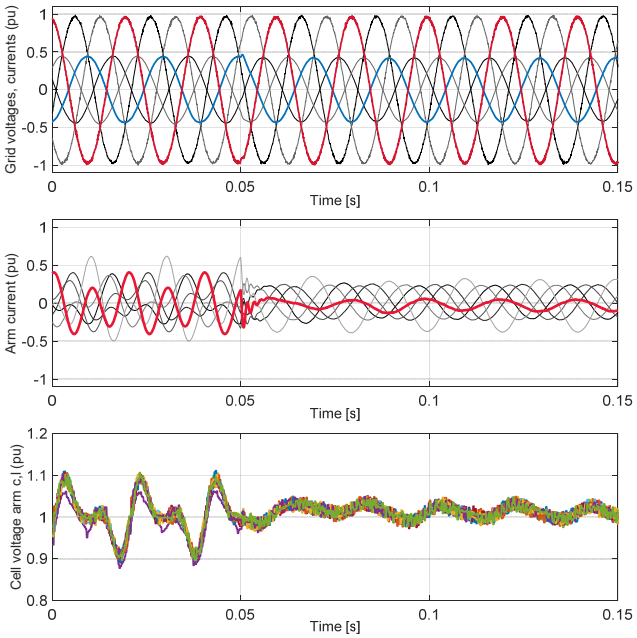

Fig. 22. Experimental results for a load step resulting in transition from a significant intra-arm unbalance to no arm unbalance.

system initially operates in a stable condition with enabled 2nd harmonic injection and the cell voltages appear bounded and well controlled. At t = 0.05 s the 2nd harmonic reference is disabled, leading to lower arm currents. Consequently, the cell capacitor voltages in the unbalanced arms start to diverge with the unloaded cells progressively charging while the loaded cells discharge. The effect will obviously affect the quality of the output voltage and the controllability of the converter. The converter will eventually stop due to overvoltage in the unloaded cells if the condition is not reverted. Reestablishing the 2nd harmonic injection after 0.1 s allows the intra-arm balancing to be again effective and the cell voltages return to their initial range.

D. Transient response to load connection or disconnection

A last test aims at verifying the transient response in case of sudden connection or disconnection of a load. This represent a condition when the charging of a vehicle battery is started or stopped. Most such load variations cause relatively smooth changes in the required second harmonic injection. However, there are some cases when a discontinuity occurs, and the transient becomes more severe. Instances of such cases are analyzed in the experiments reported in Fig. 21 and Fig. 22.

In Fig. 21, the initial condition corresponds to a case with no intra-arm unbalance in any of the arms, thus requiring no 2nd harmonic current injection for ensuring voltage balancing capability. In particular, the cells in the arm *c,l* are all unloaded, while all the cells in the remaining five arms are loaded equally with 0.5 pu. At 0.05 s, one of the cells in the unloaded arm *c,l* is loaded with 1.0 pu, resulting in maximum intra-arm unbalance, requiring considerable 2nd harmonic injection. The results highlight that the transient response is well controlled and does not present significant overshoots or undamped oscillations. The unbalance does result in higher arm currents and larger oscillations in the cell voltages, but the grid-side voltages and currents are almost unaffected, with only a marginal increase of distortion.

The experiment of Fig. 22 demonstrates the response to the reverse load change, resulting in a change of operation from a situation with severe intra-arm unbalance to one with no intra arm unbalance at all. The behavior of the system is symmetrical to the case described before, with all internal and external variables being properly controlled.

IX. CONCLUSIONS

A system configuration enabling transformer-less grid connection of large-scale infrastructures for wireless charging of electric vehicles (EVs) was presented in this paper. The proposed configuration is based on a modular multilevel converter (MMC) topology where each module supplies a wireless EV charger. This solution offers several potential advantages compared to conventional ac distribution to each charging unit, including reduced length and cross section of cables, reduced need for ac-side filtering, and scalable design for direct transformer-less connection to medium voltage (MV) grids. These characteristics could allow for reduced footprint and cost of large-scale charging infrastructures in space constrained urban areas. The presented topology takes advantage of the inherent galvanic isolation of wireless EV chargers, but the same concept could also be utilized for other applications with a high number of individual, galvanically isolated, loads.

The operation of an MMC with unequal loading on the modules requires active balancing control for regulating the internal capacitor voltages. As a main contribution of the paper, the requirements for intra-arm balancing with individually loaded modules are identified and analyzed. It is

shown that the balancing capability depends on the intra-arm load unbalance and the arm current, which in turn depends on the total load and the circulating currents required for balancing the aggregated loads of the different arms. It is also demonstrated how the intra-arm balancing capability can be increased by introducing a second harmonic component of the circulating current. The required second harmonic current component and its impact on the total arm currents are quantified to provide a load-dependent circulating current reference that can ensure operability of the MMC under any loading conditions. This analysis is critical for the proposed MMC-based charging infrastructure but is also applicable for any other applications of MMCs with individually loaded modules.

The validity of the analysis presented in the manuscript and the operation of the proposed control strategy for load balancing have been verified numerically by time domain simulations and experimentally with a small-scale laboratory setup. The results demonstrate that the proposed configuration can handle extreme unbalanced conditions, but also show how this unbalance can translate into requirements for very high circulating currents and increased total current rating of the arms. However, it is demonstrated how redundancy in the number of modules can reduce the required circulating current amplitude. Furthermore, the results indicate how the most severely unbalanced conditions will rarely occur in an EV parking facility and how active scheduling strategies for keeping the unbalance within specified limits can prevent the need for increased the current rating of the system components.

REFERENCES

[1] S. Chen, Y. Ji, L. Tong, "Large Scale Charging of Electric Vehicles," in *Proceedings of the 2012 IEEE Power and Energy Society General Meeting*, San Diego, California, USA, 22-26 July 2012, 8 pp.

[2] F. Palone, M. Rebolini, S. Gentili, G. M. Giannuzzi, M. Schembari, S. Lauria, "Connection of very large public charging station to the HV transmission grid", in *Proceedings of the 2015 IEEE 15th International Conference on Environment and Electrical Engineering,* EEEIC 2015, Rome, Italy, 10-13 June 2015, pp. 1262-1267

[3] I. S Bayram, G. Michailidis, M. Devetsikiotis, "Electric Power Resource Provisioning for Large Scale Public EV Charging Facilities," in *Proceedings of the 2013 IEEE International Conference on Smart Grid Communications*, Vancouver, Canada, October 2013, pp. 133-138

[4] I. S Bayram, A. Tajer, M. Abdallah, K. Qaraqe, "Capacity Planning Framework for Electric Vehicles Charging Stations With Multiclass Costumers" in *IEEE Transactions on Smart Grid*, Vol. 6, No. 4, pp. 1934-1943, July 2015

[5] N. Neyestani, M. Y. Damavandi, M. Shafie-khah, A. G. Bakirtzis, J. P. S. Catalãõ,, "Plug-In Electric Vehicles Parking Lot Equilibria With Energy and Reserve Markets," in *IEEE Transactions on Power Systems*, Vol. 32, No. 3, pp. 2001-2016, May 2017

[6] D. Strickland, T. Embley, J. Osborne, J. Yang, Z. Qiao, A. Malhotra, A. Corliss, K. Ashworth, " Feasibility study: investigation of car park-based V2G services in the UK central hub," in *The Journal of Engineering*, Vol. 2019, No. 17, pp. 3967-3971, June 2019

[7] G. Maggetto. P. Van den Bossche, "Inductive Automatic Charging: The Way to Safe, Efficient and User-Friendly Electric Vehicle Infrastructure, in *Proceedings of the 18th International Electric Vehicle Symposium and Exhibition*, EVS-18, Berlin, Germany, 20-24 October 2001, 12 pp.

[8] M. Kane, "Wireless Charging And Autonomous Electric Cars Go Hand-In Hand", InsideEVs, 09.04.2017, https://insideevs.com/wireless-charging-autonomous-electric-cars/

[9] S. Li and C. C. Mi, "Wireless power transfer for electric vehicle applications," *IEEE Journal of Emerging and Selected Topics in Power Electronics*, Vol. 3, No. 1, pp. 4–17, March 2015.

[10] G. Guidi, S. D'Arco, J. A. Suul, R. Iso, J.-I. Itoh, "A Modular Multilevel Interface for Transformer-less Grid Integration of Large-Scale Infrastructure for Wireless Electric Vehicle Charging," in *Proceedings of the 10th International Conference on Power Electronics*, ICPE – ECCE Asia, 27-30 May, Busan, Korea, 8 pp.

[11] N. Kawakami, S. Ota, H. Kon, S. Konno, H. Akagi, H. Kobayashi, N. Okada, "Development of a 500-kW Modular Multilevel Cascade Converter for Battery Energy Storage Systems," in *IEEE Transactions on Industry Applications*, Vol. 50, No. 6, pp. 3902-3910, November/December 2014

[12] D. Ronanki, S. S. Williamson, "Modular Multilevel Converters for Transportation Electrification: Challenges and Opportunities," in *IEEE Transactions on Transportation Electrification*, Vol. 4, No. 2, pp. 399-407, June 2018

[13] T. Soong, P. W. Lehn, "Internal Power Flow of a Modular Multilevel Converter With Distributed Energy Resources," in *IEEE Journal of Emerging and Selected Topics in Power Electronics*, Vol. 2, No. 4, pp. 1127-1138, December 2014

[14] J. Khazaei, G. Pavlak, B. Lee, M. Elsenbaty, "A Novel Application of Modular Multi-Level Converters for Partially Shaded PV Systems," in *Proceedings of the 2019 IEEE Texas Power and Energy Conference*, TPEC 2019, College Station, Texas, USA, 7-8 February 2019, 6 pp.

[15] M. Mao, T. Tao, Y. Ding, J. Li, L. Chang, "Interactive Energy Management Strategy for MMC-Based EV Fleet Integrated into Smart Grid," in *Proceedings of the 2015 IEEE Energy Conversion Congress and Exposition*, ECCE 2015, Montreal, Quebec, Canada, 20-24 September 2015, pp. 4745-4752

[16] M. Mao, Y. Ding, L. Chang, N. D. Hatziargyriou, Q. Chen, T. Tao, Y. Li, "Multi-Objective Power Management for EV Fleet With MMC-Based Integration Into Smart Grid," in *IEEE Transactions on Smart Grid*, Vol. 10, No. 2, pp. 1428-1439, March 2019

[17] F. Briz, M. López, A. Rodríguez, M .Arias, "Modular Power Electronic Transformers – Modular Multilevel Converters Versus Cascaded H-Bridge Solutions," in *IEEE Industrial Electronics Magazine*, Vol. 10, No. 4, pp. 6-19, December 2016

[18] F. Briz, M. López, A. Zapico, A. Rodríguez, D. Diaz-Reigosa, "Operation and control of MMCs using cells with power transfer capability," in *Proceedings of the 30th Annual IEEE Applied Power Electronics Conference and Exposition*, APEC 2015, Charlotte, North Carolina, USA, 15-19 March 2015, pp. 980-987

[19] M. López, F. Briz, A. Zapico, A. Rodríguez, D. Diaz-Reigosa, "Control Strategies for MMC Using Cells with Power Transfer Capability" in *Proceedings of the 7th Annual IEEE Energy Covnersion Congress and Exposition*, ECCE 2015, Montreal, Quebec, Canada, 20-24 September 2015, pp. 3570-3577

[20] H. Bayat, A. Yazdani, "A Power Mismatch Elimination Strategy for an MMC-Based Photovoltaic System," in *IEEE Transactions on Energy Conversion*, Vol. 33, No. 3, pp. 1519-1528, September 2018

[21] B. S. Riar, U. Madawala, "A Modular Multi-level Converter (M2LC) based on Inductive Power Transfer (IPT) Technology, in *Proceedings of the 3rd IEEE International Conference on Sustainable Energy Technologies*, ICSET 2012, Kathmandu, Nepal, 24-27 September 2012, pp. 54-59

[22] B. S. Riar, U. K. Madawala, D. J. Thrimawithana, "Analysis and Control of a Three-phase Modular Multi-level Converter based on Inductive Power Transfer Technology (M2LC-IPT)" in *Proceedings of the 2013 IEEE International Conference on Industrial Technology*, Cape Town, South Africa, 25-28 February 2013, pp. 475-480

[23] K. Kandasamy, D. M. Vilathgamuwa, U. K. Madawala, K.-J. Tseng, "Inductively coupled modular battery system for electric vehicles," in *IET Power Electronics*, Vol. 9, No. 2, pp. 1-10, March 2016

[24] M. Yilmaz, P. T. Krein, "Review of Battery Charger Topologies, Charging Power Levels, and Infrastructure for Plug-In Electric and Hybrid Vehicles", in *IEEE Transactions on Power Electronics*, Vol. 28, No. 5, pp. 2151-2169, May 2013

[25] H. Akagi, "Classification, Terminology and Application of the Modular Multilevel Cascade Converter (MMCC)," in *IEEE Transactions on Power Electronics*, Vol. 26, No. 11, pp. 3119-3130, November 2011

[26] S. Rohner, J. Weber, and S. Bernet, "Continuous model of modular multilevel converter with experimental verification," in *Proceedings of the IEEE Energy Conversion Congress and Exposition*, Phoenix, Arizona, USA, 17-22 September 2011, pp. 4021–4028

[27] L. Harnefors, A. Antonopoulos, S. Norrga, L. Ängquist, and H.-P. Nee, "Dynamic analysis of modular multilevel converters," *IEEE Transactions on. Industrial Electronics*, Vol. 60, No. 7, pp. 2526–2537, July 2013

[28] H. Saad, X. Guillaud, J. Mahseredjian, S. Dennetière, and S. Nguefeu, "MMC capacitor voltage decoupling and balancing controls," *IEEE Transactions on Power Delivery.*, vol. 30, no. 2, pp. 704–712, April 2015

[29] G. Bergna, J. A. Suul, S. D'Arco, "State-Space Modeling of Modular Multilevel Converters for Constant Variables in Steady-State," in *Proceedings of the 17th IEEE Workshop on Control and Modeling for Power Electronics*, COMPEL 2016, Trondheim, Norway, 27-30 June 2016, 9 pp.

[30] G. Bergna-Diaz, J. Freytes, X. Guillaud, S. D'Arco, J. A. Suul, "Generalized Voltage-based State-Space Modelling of Modular Multilevel Converters with Constant Equilibrium in Steady-State," in *IEEE Journal of Emerging and Selected Topics in Power Electronics*, Vol. 6, No. 2, pp. 707-725, June 2018

[31] A. Lesnicar, R. Marquart, "An Innovative Modular Multilevel Converter Topology Suitable for a Wide Power Range," *in Proceedings of the 2003 IEEE Bologna PowerTech*, 23-26 June 2003, Bologna, Italy, pp. 272-277

[32] A. Antonopoulos, L. Ängquist, and H.-P. Nee, "On dynamics and voltage control of the modular multilevel converter," in *Proceedings of the 13th European Conference on Power Electronics and Applications*, EPE'09, Barcelona, Spain, 8-10 September 2009, 10 pp.

[33] D. Soto-Sanchez, T. C. Green, "Control of a modular multilevel converter-based HVDC transmission system," in *Proceedings of the 2011 14th European Conference on Power Electronics and Applications*, EPE 2011, Birmingham, UK

[34] J. Freytes, G. Bergna, J. A. Suul, S. D'Arco, H. Saad, X. Guillaud, "State-space modelling with Steady-State Time Invariant Representation of Energy Based Controllers for Modular Multilevel Converters," in *Proceedings of the 12th IEEE PES PowerTech Conference*, Manchester, UK, 18-22 June 2017, 7 pp.

[35] S. Fuchs, S. Beck, J. Biela, "Analysis and Reduction of the Output Voltage Error of PWM for Modular Multilevel Converters," in *IEEE Transactions on Industrial Electronics*, Vol. 66, No. 3, pp. 2291-2301, March 2019

[36] E. Gümrükcü, F. Ponci, A. Monti, G. Guidi, S. D'Arco, J. A. Suul, "Optimized Application of Loads in MMC-based Electric Vehicle Charging Infrastructure," in *Proceedings of the 2020 IEEE International Conference on Power System Technology*, POWERCON 2020, Bangalore, India / Virtual Conference, 14-16 September 2020, 6 pp.

[37] S. D'Arco, G. Guidi, J. A. Suul, "Operation of a Modular Multilevel Converter Controlled as a Virtual Synchronous Machine," in *Proceedings of the International Power Electronics Conference*, IPEC 2018 ECCE Asia, Niigata, Japan, 20-24 May 2018, 8 pp.

[38] K. Ljøkelsøy, G. Guidi, "Development of a scaled model of a modular multilevel converter," in *Energy Procedia*, Vol. 137, 2017, pp. 505-513.

Giuseppe Guidi (M'00, SM'20) received the Graduate degree from the University of L'Aquila, L'Aquila, Italy, in 1995, and the Ph.D. degree from the Norwegian University of Science and Technology (NTNU), Trondheim, Norway, in 2009.

He was involved in the field of power electronic drives from 1997 to 2004, joining first Fuji Electric R&D, Japan, as R&D Engineer and then SIEI SpA, Italy, as a Senior Engineer. In 2009, he joined Yokohama National University, Yokohama, Japan, as a Research Associate, working on power converters for electric vehicles. From 2011 he was a part-time Research Associate with NTNU, until joining SINTEF Energy Research, Trondheim, Norway, in 2013. His current research interests include power electronics, traction control, and drive systems for electric propulsion, as well as application of power electronics to renewable energy.

Salvatore D'Arco received the M.Sc. and Ph.D. degrees in electrical engineering from the University of Naples "Federico II," Naples, Italy, in 2002 and 2005, respectively.

From 2006 to 2007, he was a postdoctoral researcher at the University of South Carolina, Columbia, SC, USA. In 2008, he joined ASML, Veldhoven, the Netherlands, as a Power Electronics Designer, where he worked until 2010. From 2010 to 2012, he was a postdoctoral researcher in the Department of Electric Power Engineering at the Norwegian University of Science and Technology (NTNU), Trondheim, Norway. In 2012, he joined SINTEF Energy Research where he currently works as a Senior Research Scientist. He is the author of more than 100 scientific papers and is the holder of one patent. His main research activities are related to control and analysis of power-electronic conversion systems for power system applications, including real-time simulation and rapid prototyping of converter control systems.

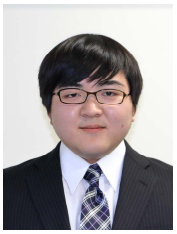

Kodai Nishikawa was born in Niigata, Japan, in 1997. He received the B.S. degree in electrical, electronics and information engineering in 2020 from Nagaoka University of Technology, Niigata, Japan, where he is currently working towards the Ph.D. degree.

From October 2019 to February 2020 he was an internship-student at SINTEF Energy Research, Trondheim, Norway. His current research interests include optimization methods of passive components for large-capacity single-phase AC-AC converters. Mr. Nishikawa is a student member of the Institute of Electrical Engineers of Japan.

Jon Are Suul (M'11) received the M.Sc. degree in energy and environmental engineering and the Ph.D. degree in electric power engineering from the Norwegian University of Science and Technology (NTNU), Trondheim, Norway, in 2006 and 2012, respectively.

From 2006 to 2007, he was with SINTEF Energy Research, Trondheim, where he was working with simulation of power electronic converters and marine propulsion systems until starting his Ph.D. studies. Since 2012, he has been a Research Scientist with SINTEF Energy Research, first in a part-time position while working as a part-time Postdoctoral Researcher with the Department of Electric Power Engineering of NTNU until 2016. Since August 2017, he has been an Adjunct Associate Professor with the Department of Engineering Cybernetics, NTNU. His research interests are mainly related to modeling, analysis, and control of power electronic converters in power systems, renewable energy applications, and electrification of transport.s